

Thesis

Ekaterina Avdeeva

University of Nebraska-Lincoln, USA

December 12, 2016

Abstract

This paper reviews

Contents

8	1	Introduction	2
9	1.1	Fundamental Particles and Interactions	3
10	1.2	Electroweak Interactions	5
11	1.3	Strong Interactions	8
12	1.4	Physics of Proton-Proton Collisions	9
13	1.5	Open Questions of the Standard Model	11
14	2	$W\gamma$ Production Theory and Former Experimental Results	12
15	2.1	Electroweak Theory of the Standard Model	13
16	2.2	Cross Section and Luminosity	18
17	2.3	Standard Model $W\gamma$ Production	20
18	2.4	Anomalous $W\gamma$ Production	22
19	2.5	Measurements in the Past	25
20	3	Experimental Setup	27
21	3.1	Large Hadron Collider	28
22	3.2	Compact Muon Solenoid	31
23	3.2.1	Introduction	31
24	3.2.2	Magnet	32
25	3.2.3	Tracking System	32
26	3.2.4	Electromagnetic Calorimeter	33
27	3.2.5	Hadron Calorimeter	34
28	3.2.6	Muon System	34
29	3.2.7	Triggering and Data Aquisition	35
30	3.2.8	Event Reconstruction	35
31	4	CMS Tracker Alignment	38
32	4.1	Algorithm	39
33	4.2	Selected Results	44
34	5	$W\gamma$ Cross Section Measurement	45

35 1 Introduction

36 Elementary particle physics describes our world in terms of its smallest constituents which are
37 called fundamental particles, and their interactions. When examined at smaller scales, the sub-
38 stances around us consist of molecules, molecules consist of atoms. In an atom there is a nucleus
39 made of neutrons and protons and some number of electrons occupying their orbits around
40 the nucleus. Protons and neutrons have a structure while an electron is not known to have any
41 structure, therefore, an electron is an example of a particle which is considered to be fundamental.

42 Interactions of elementary particles are described by quantum field theories which incorporate
43 principles of the quantum mechanics and the special theory of relativity. The set of such theories,
44 including quantum electrodynamics (QED), quantum chromodynamics (QCD) and the theory
45 of weak interactions is called the Standard Model (SM). It has been proven to be an accurate
46 description of interactions of elementary particles observed by now.

47 However, there are several experimental observations that are not described by the SM such
48 as effects of gravity, dark matter, dark energy, matter/antimatter asymmetry and others. There-
49 fore, the SM is not the complete theory of particle interactions. There are several SM extensions
50 offered by theorists as well as radically new theories waiting for the experimental confirmation
51 or disproof.

52 Some SM extensions and new theories predict the existence of heavy particles mass of which
53 possibly lies beyond experimentally reachable energies. The search of these particles is one of the
54 prioritized directions in particle physics. One source of highly energetic elementary particles is
55 cosmic rays. The most energetic particles ever observed came from this source. However, cosmic
56 rays are totally uncontrollable and such highly energetic particles are rare. If we want to produce
57 a large number of particles in a given energy range, we need to use a particle accelerator. A
58 large amount of data allows experimentalists to perform a statistical analysis and increase the
59 probability to find a new particle if it exists.

60 Symmetric colliding beams is the most effective way to produce as heavy particles as possible
61 given the energies of the colliding particles. Comparing to experiments of colliding a single beam
62 to a fixed target, in case of a symmetric collision the total momentum of two colliding particles
63 is zero and, therefore, much larger fraction of energy can transfer to a mass of a new particle.
64 The Large Hadron Collider (LHC) is such a collider with the highest energy in the world ever
65 built. It can produce the most massive particles to probe physics beyond the SM. It collides two
66 proton ($p p$) beams, two lead ion beams ($Pb - Pb$) or a proton beam to a lead ion beam ($p - Pb$).
67 The design energies for a colliding proton and a colliding lead ion at LHC are 7 TeV and 522 TeV
68 respectively.

69 Compact Muon Solenoid (CMS) is one of two general-purpose detectors at the LHC. It is
70 placed at one of six collision points. CMS has a wide physics program including searches for
71 the beyond SM (BSM) physics as well as the precision measurements of the parameters of the
72 SM itself. The measurement of this dissertation is a SM measurement with CMS data collected
73 in 2012 in $p p$ collisions of LHC with beam energies of 4 TeV. The result can be compared to the
74 SM prediction. Certain BSM theories predict a deviation of the result of this measurement from
75 its SM value, therefore, with this measurement, in addition to testing the SM, we also search for
76 a new physics.

77 The rest of this chapter gives general introductory information about the SM while Ch. 2
78 concentrates on the theory of the SM and BSM $W\gamma$ production and also discusses previous
79 measurements of this process. Chapter 3 describes LHC and CMS in more details. Chapter 4
80 explains one specific detail of the CMS operation that is the spacial alignment of the tracking
81 detector of charged particles in CMS. Finally, Ch. 5 describes the details of the measurement of
82 this dissertation and reports the results.

90 1.1 Fundamental Particles and Interactions

91 The SM describes interactions of elementary particles. There are four fundamental interactions:
92 electromagnetic, strong, weak and gravitational. The gravity is not included into the SM but its
93 effect on particles is negligible compared to the other forces which makes it possible to develop a
94 theory of the particle physics and conduct experiments even without having the gravity included
95 into the model.

96
97 All fundamental elementary particles in the SM can be split into three categories by their
98 spins. There are fermions which possess spin $s=1/2$, there are gauge bosons which are vector
99 particles ($s=1$) and there is the Higgs boson which is a scalar particle ($s=0$).

100
101 The fermions are arranged into three generations, each generation consists of a quark with
102 charge $Q=+2/3$ (up, charm, and top quarks), a quark with $Q=-1/3$ (down, strange, and bottom
103 quarks), a charged lepton with $Q=-1$ (electron, muon, and tau-lepton) and a neutrino (electron,
104 muon, and tau neutrinos) which is electrically neutral. Each quark can carry any of three colors:
105 red, blue, or green. Additionally, each fermion has its antiparticle. Therefore, the total number
106 of fundamental fermions is $(6(\text{leptons}) + 6(\text{quarks}) \cdot 3(\text{colors})) \cdot 2(\text{to include antiparticles}) = 48$.

107
108 Corresponding particles in different generations have the same charges, spins and interaction
109 properties but masses of particles increase with a generation. These mass differences lead
110 to different decay properties because a particle A can decay to particles B and C only if their
111 masses relate as $m_A > m_B + m_C$. Thus, an electron is a stable particle, a muon decays as
112 $\mu^- \rightarrow e^- + \bar{\nu}_e + \nu_\mu$, a tau-lepton, as the heaviest charged lepton, has the largest number of decay
113 channels amongst the charged leptons: $\tau^- \rightarrow \mu^- + \bar{\nu}_\mu + \nu_\tau$, $\tau^- \rightarrow e^- + \bar{\nu}_e + \nu_\tau$, $\tau^- \rightarrow \nu_\tau + \text{quarks}$.

114
115 In addition to fermions, the SM includes gauge bosons which are interaction mediators. They
116 are called mediators because fermions interact with each other by exchanging them. For example,
117 two charged fermions can interact with each other by exchanging a photon. Such interaction is
118 called electromagnetic interaction and a photon is a mediator for the electromagnetic interaction.
119 Similarly, a gluon is a mediator for strong interactions, and W^\pm and Z^0 bosons are mediators
120 for weak interactions. W^\pm and Z^0 bosons are massive while a photon and a gluon are massless
121 particles.

122
123 The last SM particle is the Higgs boson. The Higgs boson is a scalar neutral particle which
124 is playing a critical role in the electroweak symmetry breaking. The Higgs mechanism explains
125 how W and Z bosons become massive particles.

126
127 All the particles are summarized in Fig. 1. These and only these fundamental particles and
128 their antiparticles have been discovered by now. However, there are many composite particles
129 which are called hadrons. Hadrons can consist of three quarks (baryons), quark and antiquark
130 (meson), or three antiquarks (antibaryons). Hadrons always possess an integer charge.

131
132 Most of the particles are short-lived and decay within microseconds. The only stable particles
133 are protons and antiprotons, electrons and positrons, neutrinos and antineutrinos, photons,
134 and, in some sense, gluons. However, if a particle cannot decay, it does not mean that it would
135 live forever. There are many different kinds of reactions in which particles can disappear. An-
136 tiprotons and positrons would immediately annihilate with protons and electrons, photons can
137 be absorbed by charged particles, electrons and protons can scatter to produce neutrons and
138 neutrinos and many other reactions are possible.

139
140 In this dissertation, the study of $pp \rightarrow W\gamma + X$ process where the W decays as $W \rightarrow \ell\nu$
141 where $\ell = e, \mu$ is reported. The $W\gamma$ production with leptonic W decays proceeds through one of
142 the following three processes: the initial state radiation where a photon is emitted from one of
143 the incoming partons, the final state radiation where a photon is radiated off the charged lepton
144 from the W boson decay, and, finally, the triple gauge coupling (TGC) where a photon is emitted

from the W boson. Many BSM theories predict an enhancement of the TGC production over the SM value and, therefore, the experimental search for such an enhancement is a good test for such theories.

148

Therefore, the focus of this study is an interaction between a photon and a W boson however many other SM particles are relevant too. Thus, a charged lepton and a neutrino appear as the final state particles, a quark and an antiquark appear as initial state particles and all fundamental particles except the Higgs boson participate in various background processes. Subsections 1.2-1.4, chapter 2 and [1] describe particle interactions in more details.

154

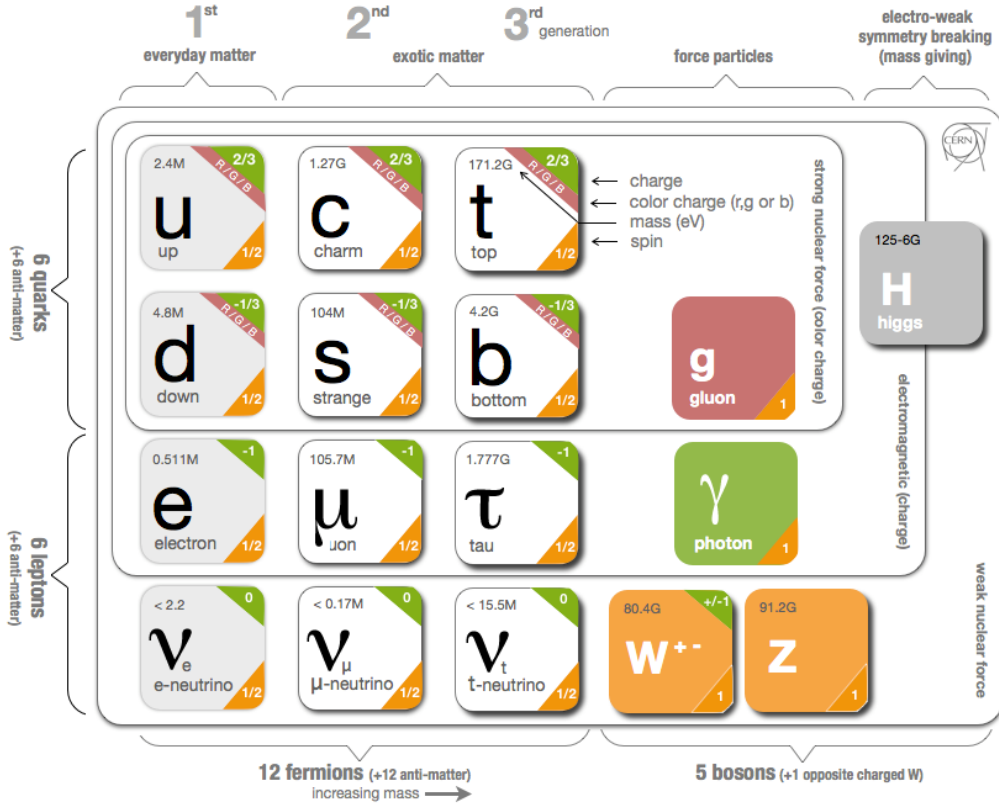


Figure 1: Standard Model Particles and Interactions. Source of the figure: [2].

155 **1.2 Electroweak Interactions**

156 All electrically charged particles participate in electromagnetic interactions. All electromagnetic
 157 interactions are mediated by a photon, a spin-one electrically neutral massless particle, and can
 158 be reduced to one elementary process (Fig. 2, left). This process represents a charged fermion
 159 radiating or absorbing a photon. Such elementary process itself is forbidden by the energy con-
 160 servation law but this element is a base of actual process. For example, the Bhabha scattering,
 161 $e^+e^- \rightarrow e^+e^-$, occurs through e^+e^- annihilation with further production of a new e^+e^- pair
 162 (Fig. 2, middle) or through exchange of a photon between the positron and the electron (Fig. 2,
 163 right). Both cases involve nothing except the elementary process (Fig. 2, left). Such graphical
 164 representations of the particle physics processes are called Feynman diagrams.

165

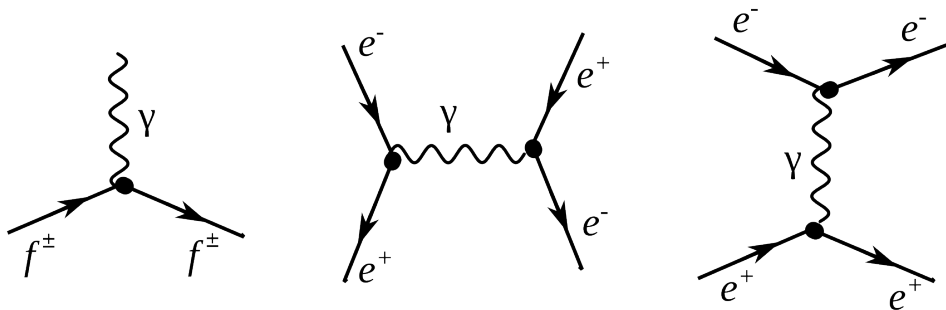


Figure 2: Electromagnetic interactions

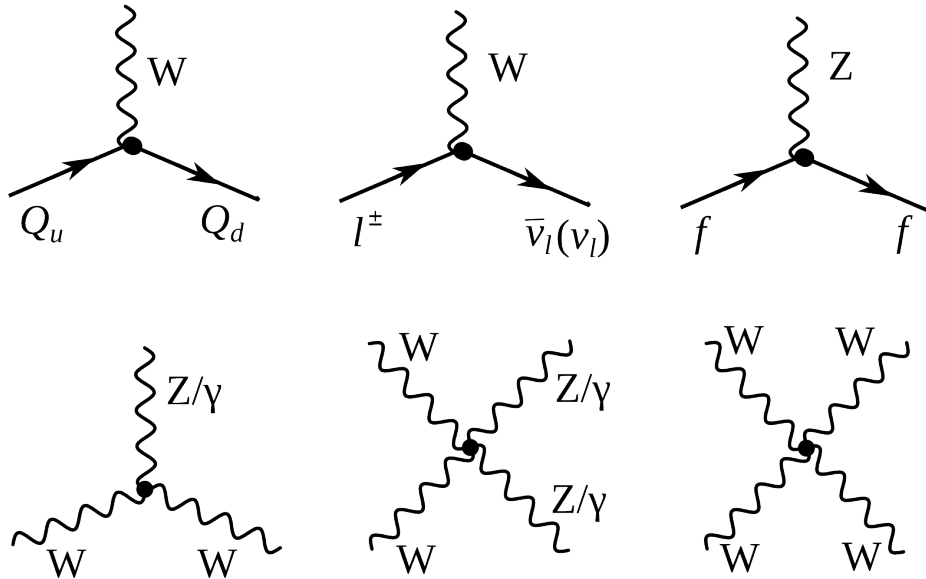


Figure 3: Weak elementary processes and gauge couplings

166 As for the weak interactions, there are two kinds of them: neutral (mediated by a Z boson)

and charged (mediated by a W^\pm boson). Elementary processes with W and Z bosons are shown in Fig. 3. Because the electric charge must be conserved at any vertex, a particle radiating or absorbing a W boson converts to a different particle. Thus, a charged lepton converts to a neutrino (or vice versa) as shown in Fig. 3, top left. Each lepton carries a lepton flavor number (Tab. 1). A lepton flavor number is conserved in any interaction, thus an electron radiating a W boson always converts to an electron neutrino, a muon converts to a muon neutrino etc.

173

Table 1: Lepton Flavor Number

particles	L_e	L_μ	L_τ
e^-, ν_e	+1	0	0
$e^+, \bar{\nu}_e$	-1	0	0
μ^-, ν_μ	0	+1	0
$\mu^+, \bar{\nu}_\mu$	0	-1	0
τ^-, ν_τ	0	0	+1
$\tau^+, \bar{\nu}_\tau$	0	0	-1

From top middle diagram in Fig. 3 we see that if a quark with $Q=-1/3$ enters, then a quark with $Q=+2/3$ escapes and, therefore, the flavor of the quark is changed. The charged weak interaction is the only interaction which changes a quark flavor. The probability of each of three quarks with $Q=+2/3$ to be born is determined by the Cabibbo-Kobayashi-Maskawa matrix which relates mass eigenstates d, c and b to weak eigenstates d', c' and b' (Eq. 1). Absolute values of the matrix elements are all known (Eq. 2) and are the highest for the quark of the same generation as an initial state quark. In the particular case shown in the top middle diagram in Fig. 3, d is the initial state quark and u has the highest probability to be produced after an interaction with a W boson but c and t can also be produced if there is enough energy.

183

$$\begin{pmatrix} d' \\ s' \\ b' \end{pmatrix} = \begin{pmatrix} V_{ud} & V_{us} & V_{ub} \\ V_{cd} & V_{cs} & V_{cb} \\ V_{td} & V_{ts} & V_{tb} \end{pmatrix} \begin{pmatrix} d \\ s \\ b \end{pmatrix} \quad (1)$$

$$\begin{pmatrix} |V_{ud}| & |V_{us}| & |V_{ub}| \\ |V_{cd}| & |V_{cs}| & |V_{cb}| \\ |V_{td}| & |V_{ts}| & |V_{tb}| \end{pmatrix} = \begin{pmatrix} 0.97 & 0.23 & 0.00 \\ 0.23 & 0.97 & 0.04 \\ 0.01 & 0.04 & 1.00 \end{pmatrix} \quad (2)$$

An elementary process of a neutral weak interaction is an emission of a Z boson off a fermion line (right top diagram in Fig. 3). An electron is shown here as an example however it could also be any lepton, antilepton, quark or antiquark. Diagrams with a Z boson are very similar to ones with a photon except a photon can only be radiated off a charged particle but a Z boson can also be radiated off a neutrino or antineutrino.

189

The bottom diagrams in Fig. 3 are gauge bosons coupling diagrams including self-coupling of a W boson, its interaction with a Z boson and its electromagnetic radiation of a photon. Charge-conserving triple and quartic gauge couplings containing two or four W bosons are all possible in the SM: WWZ , $WW\gamma$, $WWZZ$, $WWZ\gamma$, $WW\gamma\gamma$, and $WWWW$.

194

Electromagnetic and weak interactions are unified by the electroweak Glashow-Weinberg-Salam (GWS) theory which is based on $SU(2) \times U(1)$ symmetry. $SU(2)$ is the symmetry of weak isospin which generates three bosons: W^1 , W^2 and W^3 . $U(1)$ is the symmetry of the weak

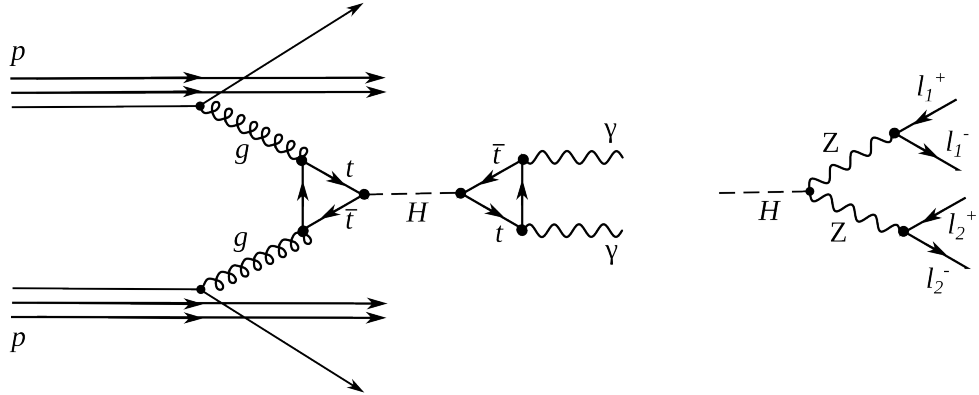


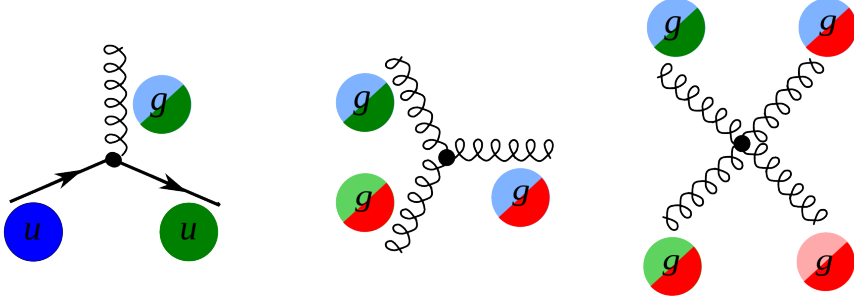
Figure 4: The Higgs boson production and decay

198 hypercharge and generate one neutral boson B . W^1 and W^2 are mixed to create W^+ and W^-
199 mediators while W^3 and B are mixed to create a Z boson and a photon. Therefore, the GWS
200 theory considers electromagnetic and weak forces as different manifestations of the electroweak
201 force. The electroweak theory is discussed in greater details in Ch. 2.

202
203 However, weak interactions are mediated by heavy bosons ($M_W = 80$ GeV, $M_Z = 91$ GeV)
204 while electromagnetic interactions are mediated by a massless photon, thus, the electroweak
205 symmetry is broken. To explain this phenomenon, the Higgs mechanism was introduced. The
206 mechanism predicted an existence of an additional boson: the Higgs boson. The Higgs boson
207 was a missing piece of the SM for many years and was finally discovered in 2012 at LHC by
208 ATLAS and CMS collaborations through the processes shown in Fig. 4 [3], [4].

209
210 The measurement in this dissertation is an electroweak measurement because the process in-
211volves a W boson. It includes an interaction of a W boson with leptons and quarks as well as the
212 triple gauge coupling $WW\gamma$. Thus, the measurement is a good test of the SM electroweak theory.
213

214 1.3 Strong Interactions



215 Figure 5: Elementary processes of strong interactions

216 The third fundamental force after the electromagnetic and weak ones is the strong force. The
 217 strong force is responsible for glueing protons and neutrons together in the nuclei as well as for
 218 forming protons and neutrons themselves. The strong interactions occur by exchanging gluons
 219 which are spin-one massless electrically neutral particles.

220 The elementary strong processes are shown in Fig. 5. There are three elementary processes:
 221 qqg , ggg and $gggg$, all are involving particles with color charges. Thus, gluons couple to quarks
 222 and self-couple. Color charges must be conserved at each elementary process of the strong inter-
 223 action. Each quark possesses one of three colors at a time, and there are eight types of gluons
 224 to cover all possible color exchanges.

225 The coupling constant of the strong interaction depends on a distance between interacting
 226 particles: it becomes larger as the distance becomes larger and smaller as the distance becomes
 227 smaller. As the distance approaches zero, the coupling constant approaches zero too, and, thus,
 228 in the asymptotic limit two quarks located at the same place do not interact. This property is
 229 called asymptotic freedom.

230 On the other hand, when the distance between quarks becomes larger, the coupling constant
 231 also becomes larger. This property confines quarks to always stay in the color neutral combi-
 232 nations (hadrons), it forbids the existence of free quarks. A combination becomes color neutral
 233 when there is the same amount of color and anticolor or if there is the same amount of each of
 234 the three colors. Thus, mesons are comprised of a quark and an antiquark with the opposite
 235 color charges, and baryons are comprised of three quarks: red, green and blue one. Examples of
 236 baryons include such well-known particles as a proton and a neutron.

237 The asymptotic freedom and the confinement are properties that are specific for strong inter-
 238 actions. The theory of strong interactions is called the QCD which is a quantum field theory
 239 invariant under $SU(3)$ color transformations. When the coupling constant is much less than one
 $\alpha_s \ll 1$, the perturbative approach can be used to compute observables.

240 The $W\gamma$ process being measured in this dissertation is not intended to test QCD, but a good
 241 understanding of QCD is essential for performing this measurement because the QCD corrections
 242 to the Feynman diagrams of the process are large and has to be taken into account in produc-
 243 ing simulation. In addition, QCD describes the dynamics of quarks and gluons within colliding
 244 protons and predicts probabilities of one or another quark-antiquark pair to interact. Physics of
 245 proton-proton collisions is discussed in the subsection 1.4.

1.4 Physics of Proton-Proton Collisions

Consider a pp collision at LHC. The proton energies are so high that each proton behaves as a complex structure. A proton is a baryon, it consists of three quarks: uud . These three quarks are called valence quarks. They interact with each other by exchanging gluons which produce virtual $q\bar{q}$ pairs (Fig. 6). Such quarks are called sea quarks.

Any parton from one proton can interact with any parton from another proton. Probabilities $f_i(x, Q^2)$ of any particular constituent i to interact are described partially by QCD and partially by experimental measurements and depend on the momentum transfer Q and the momentum fraction of a specific parton x . These probabilities are called parton distribution functions (PDFs).

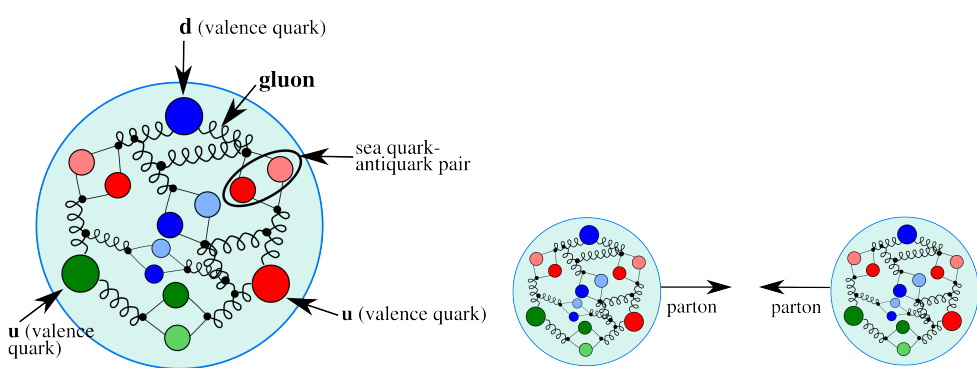


Figure 6: The proton structure (left) and the proton-proton collision (right).

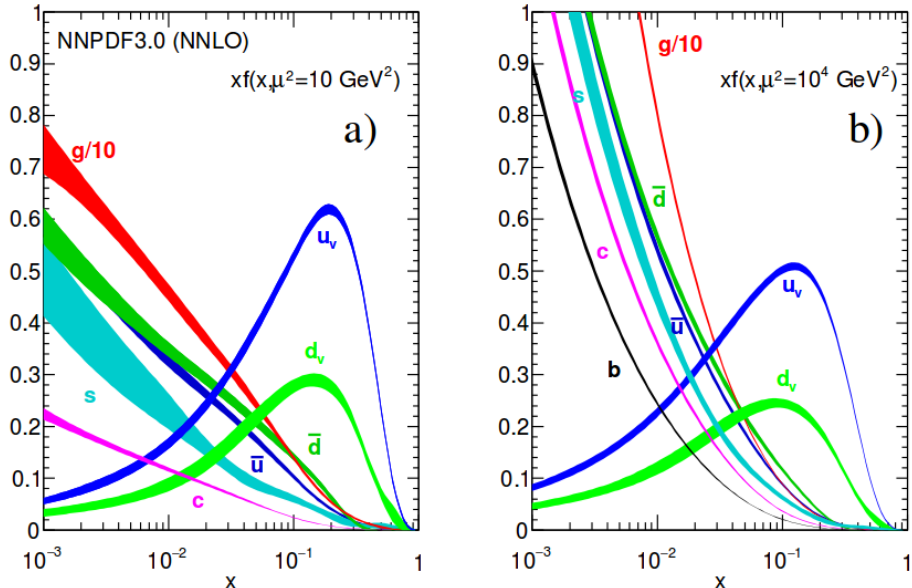


Figure 7: Parton distribution functions [5].

For large Q^2 and x gluon-gluon interactions have the largest probabilities to occur (Fig. 7).

265 However, gluons do not couple directly to a W boson, thus, in the $W\gamma$ measurement we are
266 mostly interested in quark-antiquark pairs which would have a total charge corresponding to the
267 charge of a W boson (± 1). Since we have u and d as valence quarks and we know that the
268 probability to couple to the same generation quark in charged weak interactions is the highest,
269 most of the W bosons are created by $u\bar{d}$ and $d\bar{u}$ pairs however other $q\bar{q}'$ combinations with the
270 total charges of ± 1 are also possible. The antiquarks come from virtual $q\bar{q}$ pairs inside of each
271 proton.

272
273 As we look for events containing $W\gamma$ we also have other events mimicking our process. Such
274 background events can be produced by any pair of partons.
275

276 1.5 Open Questions of the Standard Model

277 While the SM is an accurate description of all particle physics experimental results, there are
278 certain phenomena which are not included into the SM. In this subsection we discuss some of
279 them.

280 The gravitational interactions do not fit into the SM. It is the open question whether the
281 quantum theory of gravity is possible and whether there is a mediator of the gravitational in-
282 teractions. Also, it is not known why the gravitational force is so much weaker than any other
283 force. One possible explanation comes from a theory which predicts extra spatial dimensions
284 beyond the three we are dealing with (e.g. the string theory). In this case, it is possible that the
285 gravitational force is shared with other dimensions and that is why the fraction available in our
286 three dimensions is that small.

288 Another mystery of the Universe is its composition: it is known from the studies of the grav-
289 itational effects that our Universe consists of dark energy by 68%, of dark matter by 27% and of
290 baryon matter only by 5% [6]. The dark energy resists the gravitational attraction and acceler-
291 ates the expansion of the Universe, and is not detectable by any effects except gravitational. The
292 understanding of the dark energy is a question of the general relativity rather than the particle
293 physics. The dark matter however likely consists of particles and therefore is a subject of the
294 particle physics. It does not radiate and that is why it cannot be detected by telescopes. The
295 nature of the dark matter is not known but its constituents must be very stable to remain since
296 the Big Bang. The theory of the supersymmetry which is unifying fundamental particles and
297 mediators predicts many of new heavy particles and the lightest supersymmetric particle, the
298 neutralino, is a good candidate for the dark matter.

300 One more open question is the reason for the matter/antimatter asymmetry. The matter
301 and antimatter should have been created in the same amount at the moment of the Big Bang.
302 Then most of it has annihilated but because of asymmetry, there was more matter than anti-
303 matter which led to the state of the Universe we observe now. There is a phenomenon of
304 the CP-violation in weak interactions observed and described that predicts the asymmetry at
305 a certain level. However, the effect of the CP-violation is not large enough to account for the
306 observed amount of the matter and, therefore, the total matter/antimatter asymmetry remains
307 unexplained.

309 The measurement of the photon transverse momentum spectrum (P_T^γ) of the $W\gamma$ process has
310 a goal to both test the SM and search for the BSM physics. The low P_T^γ region is not expected
311 to be affected by any new physics and must agree well with the SM predictions while the high
312 P_T^γ region may indicate an existence of a new physics if there is an enhance over the SM pre-
313 dictions. The enhance would be an indirect evidence of the BSM particles like supersymmetric
314 particles or additional gauge bosons which could be part of the explanation of the dark matter
315 presence or difference in magnitudes of different interactions. More theoretical details about the
316 SM descriprion of $W\gamma$ process as well as the possible BSM physics are given in the chapter 2.

319 **2 $W\gamma$ Production Theory and Former Experimental Re-**

320 **sults**

321 Chapter 2 provides deeper theoretical background for the measurement of this dissertation and
322 discusses former experimental results. The derivation of the electroweak Lagrangian is described
323 in Ch. 2.1, including the appearance of TGC and QGC terms. Then concepts of the cross section
324 and the luminosity are discussed in Ch. ???. More specific details regarding the SM cross section
325 of $W\gamma$ are summarized in Ch. ???. Possible causes and potential effects of aTGC are explained in
326 Ch. 2.4. Finally, Ch. ?? lists former physics experiments which probed the same aTGC vertex
327 which is probed in the measurement of this dissertation including measurements of exactly the
328 same process at lower LHC beam energy.

329

330 2.1 Electroweak Theory of the Standard Model

331 To develop a quantum field theory, we start with the Lagrangian of free fermions. In order
332 to describe a system with a conservation of a physical quantity, the Lagrangian is required to
333 satisfy a local invariance with respect to a certain transformation. For instance, a conservation
334 of an electric charge requires a local invariance under $U(1)$ transformation for the QED La-
335 grangian [7]. The requirement of the local invariance introduces an interaction of a new vector
336 field (or several fields) with our free fermions. The new vector field is a mediator of an inter-
337 action conserving the physical quantity. To provide a full description for a new boson field, in
338 addition to the interaction term we introduce an invariant term for the kinetic energy of the bo-
339 son. Such approach allows us to derive the Lagrangian which is locally invariant with respect to
340 a certain gauge transformation and contains interacting fermions as well as interaction mediators.

341
342 The SM is a quantum field theory invariant under the local $SU(3)_C \times SU(2)_L \times U(1)_Y$ trans-
343 formation [7]. The SM Lagrangian includes all observed quantum fields and their interactions.

344
345 The part of the SM Lagrangian based on the $SU(3)_C$ symmetry and is called QCD or theory
346 of strong interactions. QCD has three types of charges which are called colors: red, blue, and
347 green. To be a subject of strong interaction, a fermion must posses a color charge. Quarks
348 and antiquarks are such fermions. The requirement to satisfy the gauge invariance with respect
349 to $SU(3)_C$ transformations generates eight massless gluons, and the non-abelian nature of the
350 $SU(3)$ group generates self-interactions of gluons including three-gluon and four-gluon vertices.

351
352 The part of the SM Lagrangian based on the $SU(2)_L \times U(1)_Y$ symmetry is a foundation of the
353 unified theory of electroweak interactions. $SU(2)_L$ reflects transformations in the weak isospin
354 space of left-handed fermions ([1], Ch. 9) while $U(1)_Y$ reflects transformations in a weak hyper-
355 charge space of all fermions. The requirement of the local gauge invariant generates four massless
356 vector bosons which are mediators of electromagnetic and weak interactions. The non-abelian
357 structure of $SU(2)$ group generates gauge boson self-couplings the same way as self-interactions
358 of gluons appear in QCD.

359
360 Mass terms for the vector bosons would violate the gauge invariance of the electroweak La-
361 grangian, however it is experimentally known that mediators of weak interactions are heavy
362 particles with masses $M_W = 80$ GeV and $M_Z = 91$ GeV. A possible solution of the discrepancy
363 is a mechanism of the spontaneous symmetry breaking. QED symmetry group $U(1)$ remains
364 unbroken because a photon is massless.

365
366 The mechanism of the Spontaneous Symmetry Breaking and the appearance of the mass
367 terms for W and Z boson is realized by introducing an additional doublet of scalar fields. After
368 that, the Lagrangian is being transformed in such a way that W and Z bosons acquire masses
369 through their interactions with a new particle: a Higgs boson (H). A photon does not couple to
370 the Higgs boson remaining a massless particle.

371
372 The measurement in this dissertation provides a test for the electroweak sector of the SM. We
373 will retrace the steps of the derivation of the EWK part of the SM Lagrangian starting from terms
374 of free fermions. The resulting Lagrangian accommodates electroweak gauge bosons including
375 their self-couplings. One of these self-couplings, $WW\gamma$, is the primary focus of our measurement.

376
377 It is experimentally known that dynamics of weak interactions depends on particle's chirality
378 ([1], Ch. 4.4.1). In particular, a W boson couples to left-handed fermions and right-handed an-
379 tifermions only. A Z boson couples to both left-handed and right-handed charged fermions and
380 antifermions but only to left-handed neutrinos and right-handed antineutrinos. Given different
381 properties of left-handed and right-handed fermions, they are treated differently by the elec-
382 troweak theory. $SU(2)$ doublets are introduced for the wave functions of left-handed fermions
383 while $SU(2)$ singlets are introduced for the wave functions of right-handed fermions. Equa-
384 tions 3 and 4 show wave functions for the first generation fermions. Wave functions for the other

³⁸⁵ two generations are constructed the same way.

³⁸⁶

$$\psi_1(x) = \begin{pmatrix} u \\ d' \end{pmatrix}_L, \psi_2(x) = u_R, \psi_3(x) = d'_R. \quad (3)$$

$$\psi_1(x) = \begin{pmatrix} \nu_e \\ e^- \end{pmatrix}_L, \psi_2(x) = \nu_{eR}, \psi_3(x) = e^-_R. \quad (4)$$

³⁸⁷ The state d' in Eq. 3 is a weak eigenstate which is a linear combination of mass eigenstates d, c
³⁸⁸ and b quark's wave functions and is determined by the quark mixing matrix which is also called
³⁸⁹ Cabibbo-Kobayashi-Maskawa matrix [7]:

³⁹⁰

$$\begin{pmatrix} d' \\ c' \\ b' \end{pmatrix} = V \begin{pmatrix} d \\ c \\ b \end{pmatrix} \quad (5)$$

³⁹¹ To derive the unified electroweak Lagrangian, we start with the free fermion terms:

³⁹²

$$L_0 = \sum_{j=1}^3 i\bar{\psi}_j(x)\gamma^\mu\partial_\mu\psi_j(x), \quad (6)$$

³⁹³ where γ^μ are Dirac matrices ([1], Ch. 7.1) and $\psi_j(x)$ are wave functions determined by Eqs. 3 and 4.

³⁹⁴

³⁹⁵ The wave function ψ_1 changes under the $SU(2)_L \times U(1)_Y$ transformations in the following
³⁹⁶ way:

³⁹⁷

$$\psi_1(x) \rightarrow e^{iy_1\beta}U_L\psi_1(x), \quad (7)$$

³⁹⁸ while the wave functions $\psi_{(2,3)}(x)$ are singlets of $SU(2)_L$ and are affected only by $U(1)$ transfor-
³⁹⁹ mations:

⁴⁰⁰

$$\psi_{(2,3)}(x) \rightarrow e^{iy_{(2,3)}\beta}\psi_{(2,3)}(x). \quad (8)$$

⁴⁰¹ The transformation in the weak isospin space is defined as $U_L \equiv e^{i\sigma_i\alpha_i/2}$ where σ_i are Pauli
⁴⁰² matrices ([1], Ch. 4.2.2). Phases $\alpha_i(x)$ and $\beta(x)$ in Eqs. 7 and 8 are arbitrary functions of x , and
⁴⁰³ $y_{(1,2,3)}$ are weak hypercharges which are named analogous to electric charges in QED.

⁴⁰⁴

⁴⁰⁵ In order to satisfy the local $SU(2)_L \times U(1)_Y$ invariance, partial derivatives in Eq. 6 have to
⁴⁰⁶ be substituted with covariant derivatives:

⁴⁰⁷

$$D_\mu\psi_1(x) = [\partial_\mu - ig\tilde{W}_\mu(x) - ig'y_1B_\mu(x)]\psi_1(x) \quad (9)$$

$$D_\mu\psi_{(2,3)}(x) = [\partial_\mu - ig'y_{(2,3)}B_\mu(x)]\psi_{(2,3)}(x) \quad (10)$$

⁴⁰⁸ where g, g' are arbitrary constants,

⁴⁰⁹

$$\tilde{W}_\mu(x) \equiv \frac{\sigma_i}{2}W_\mu^i(x) = \frac{1}{\sqrt{2}} \begin{pmatrix} \sqrt{2}W_\mu^3 & (W_\mu^1 - iW_\mu^2)/\sqrt{2} \\ ((W_\mu^1 + iW_\mu^2)/\sqrt{2}) & -W_\mu^3 \end{pmatrix}, \quad (11)$$

⁴¹⁰ $B_\mu, W_\mu^1, W_\mu^2, W_\mu^3$ are four vector bosons that arise from the requirement of the Lagrangian to
⁴¹¹ be invariant under local $SU(2)_L \times U(1)$ transformations.

⁴¹²

413 The Lagrangian becomes:

414

$$L_0 \rightarrow L = \sum_{j=1}^3 i\bar{\psi}_j(x)\gamma^\mu D_\mu \psi_j(x) \quad (12)$$

415 To make new vector bosons physical fields it is necessary to add terms for their kinetic energies:

416

$$L_{KIN} = -\frac{1}{4}B_{\mu\nu}B^{\mu\nu} - \frac{1}{4}W_{\mu\nu}^i W_i^{\mu\nu} \quad (13)$$

417 where $B_{\mu\nu} \equiv \partial_\mu B_\nu - \partial_\nu B_\mu$, $W_{\mu\nu}^i \equiv \partial_\mu W_\nu^i - \partial_\nu W_\mu^i + g\epsilon^{ijk}W_\mu^j W_\nu^k$

418

419 Off-diagonal terms of \tilde{W}_μ are wave functions of charged vector bosons $W^\pm = (W_\mu^1 \mp iW_\mu^2)/\sqrt{2}$
420 while W_μ^3 and B_μ are neutral fields which are mixtures of a Z boson and a photon determined by:

421

$$\begin{pmatrix} W_\mu^3 \\ B_\mu \end{pmatrix} \equiv \begin{pmatrix} \cos\theta_W & \sin\theta_W \\ -\sin\theta_W & \cos\theta_W \end{pmatrix} \begin{pmatrix} Z_\mu \\ A_\mu \end{pmatrix} \quad (14)$$

422 where θ_W is an electroweak mixing angle, A_μ is a photon field.

423

424 In order to be consistent with QED, terms involving A_μ in the electroweak Lagrangian must
425 be equal to the corresponding terms in QED Lagrangian [7]:

426

$$L_{QED} = i\bar{\psi}(x)\gamma^\mu \partial_\mu \psi(x) - m\bar{\psi}(x)\psi(x) + qA_\mu(x)\bar{\psi}(x)\gamma^\mu \psi(x) - \frac{1}{4}F_{\mu\nu}(x)F^{\mu\nu}(x), \quad (15)$$

427 where q is electric charge of $\psi(x)$ field, $F_{\mu\nu} \equiv \partial_\mu A_\nu - \partial_\nu A_\mu$.

428

429 This requirement relates g , g' , θ_W and e as $g \sin\theta_W = g' \cos\theta_W = e$ and provides expression
430 for weak hypercharges: $y = q - t_3$, where q is the electric charge and t_3 is a z -component of the
431 weak isospin. This results in $y_1 = 1/6$, $y_2 = 2/3$, and $y_3 = -1/3$ for quarks and $y_1 = -1/2$,
432 $y_2 = 0$, and $y_3 = -1$ for leptons. A right-handed neutrino has a weak hypercharge of $y_2 = 0$. It
433 also does not have an electric charge and, as a right-handed fermion, has $t_3 = 0$ and, therefore,
434 does not couple to a W boson. Thus, a right-handed neutrino does not participate in any SM
435 interaction.

436

437 Writing \tilde{W}_μ in Eq. 13 explicitly, we obtain triple gauge coupling (TGC) and quartic gauge
438 coupling (QGC) coupling terms:

439

$$L_{TGC} = -\frac{g}{4}(\partial_\mu W_\nu^i - \partial_\nu W_\mu^i)\epsilon^{ijk}W^{\mu j}W^{\nu k} - \frac{g}{4}\epsilon^{ijk}W_\mu^j W_\nu^k(\partial^\mu W^{\nu i} - \partial^\nu W^{\mu i}) \quad (16)$$

$$L_{QGC} = -\frac{g^2}{4}\epsilon^{ijk}\epsilon^{ilm}W_\mu^j W_\nu^k W^{\mu l}W^{\nu m} \quad (17)$$

440 Substituting W_μ^i and B_μ in Eq. 16 and Eq. 17 with the wave functions of W^\pm , Z and a photon:

441

$$B_\mu = -\sin\theta_W Z_\mu + \cos\theta_W A_\mu, \quad W_\mu^3 = \cos\theta_W Z_\mu + \sin\theta_W A_\mu, \quad (18)$$

$$W_\mu^1 = \sqrt{2}(W^+ + W^-), \quad W_\mu^2 = \sqrt{2}(W^- + W^+), \quad (19)$$

442 we receive charged TGC and QGC Lagrangians in the forms of Eqs. 20 and 23.

443

444 Equation 20 involves WWZ (Eq. 21) and $WW\gamma$ (Eq. 22) interactions:

445

$$L_{TGC} = L_{TGC}^{(1)} + L_{TGC}^{(2)}, \quad (20)$$

$$L_{TGC}^{(1)} = -ie \cot \theta_W (W^{-\mu\nu} W_\mu^+ Z_\nu - W^{+\mu\nu} W_\mu^- Z_\nu + W_\mu^- W_\nu^+ Z^{\mu\nu}), \quad (21)$$

$$L_{TGC}^{(2)} = -ie (W^{-\mu\nu} W_\mu^+ A_\nu - W^{+\mu\nu} W_\mu^- A_\nu + W_\mu^- W_\nu^+ A^{\mu\nu}). \quad (22)$$

446 Equation 23 involves $WWWW$ (Eq. 24), $WWZZ$ (Eq. 25), $WWZ\gamma$ (Eq. 26), and $WW\gamma\gamma$
447 (Eq. 27) interactions:

448

$$L_{QGC} = L_{QGC}^{(1)} + L_{QGC}^{(2)} + L_{QGC}^{(3)} + L_{QGC}^{(4)}, \quad (23)$$

$$L_{QGC}^{(1)} = -\frac{e^2}{2 \sin^2 \theta_W} (W_\mu^+ W^{-\mu} W_\nu^+ W^{-\nu} - W_\mu^+ W^{\mu} W_\nu^- W^{-\nu}), \quad (24)$$

$$L_{QGC}^{(2)} = -e^2 \cot^2 \theta_W (W_\mu^+ W^{-\mu} Z_\nu Z^\nu - W_\mu^+ Z^\mu W_\nu^- Z^\nu), \quad (25)$$

$$L_{QGC}^{(3)} = -e^2 \cot \theta_W (2W_\mu^+ W^{-\mu} Z_\nu A^\nu - W_\mu^+ Z^\mu W_\nu^- A^\nu - W_\mu^+ A^\mu W_\nu^- Z^\nu), \quad (26)$$

$$L_{QGC}^{(4)} = -e^2 (W_\mu^+ W^{-\mu} A_\nu A^\nu - W_\mu^+ A^\mu W_\nu^- A^\nu). \quad (27)$$

449 In the measurement of this dissertation we probe $WW\gamma$ coupling (Eq. 22).

450

451 The unified electroweak Lagrangian discussed above involves kinetic energy terms for fermions
452 and gauge bosons as well as interactions of fermions with gauge bosons, TGC, and QGC. How-
453 ever, this Lagrangian does not contain any mass terms. Because left-handed and right-handed
454 wave functions transform differently under the electroweak symmetry, adding fermion mass terms
455 of $\frac{1}{2}m_f^2 \bar{\psi}\psi$ would violate the Lagrangian invariance and, therefore, fermion mass terms are for-
456 bidden by the $SU(2) \times U(1)$ symmetry requirement. Mass terms for gauge bosons also would
457 violate the Lagrangian invariance just as a photon mass term $\frac{1}{2}m^2 A^\mu A_\mu$ would violate $U(1)$
458 invariance of L_{QED} [1]. Therefore, Lagrangian L in Eq. 12 contains massless particles only.

459

460 However, it is known from experiments that a Z boson, a W boson and fermions are massive
461 particles and, therefore, our theory should accommodate their masses. To introduce masses into
462 the electroweak Lagrangian, an $SU(2)_L$ doublet of complex scalar fields $\phi(x)$ is added to the
463 Lagrangian:

464

$$\phi(x) \equiv \begin{pmatrix} \phi^{(+)}(x) \\ \phi^{(0)}(x) \end{pmatrix} \quad (28)$$

465 By selecting a special gauge of $\phi(x)$ it is possible to spontaneously break electroweak sym-
466 metry, generate a new scalar particle, a Higgs boson [7], and introduce mass terms for W and
467 Z bosons and charged fermions through their couplings to the Higgs boson. The strength of the
468 coupling constant is proportional to the square of the particle's mass, therefore, heavier particles
469 are more likely to interact with H , and massless particles do not couple to H .

470

471 The mechanism of generating a fermion's mass involves both left-handed and right-handed
472 components of the fermion. If our hypothesis that right-handed neutrinos do not exist is right,
473 then the Higgs mechanism does not generate neutrino masses. However, from the experiments
474 of neutrino oscillations, neutrinos are known to have masses even though they are orders of
475 magnitude smaller than those of other fermions. Several hypotheses were offered to resolve this
476 contradiction however at the moment the mechanism of neutrinos to acquire masses remain un-
477 known [5].

478

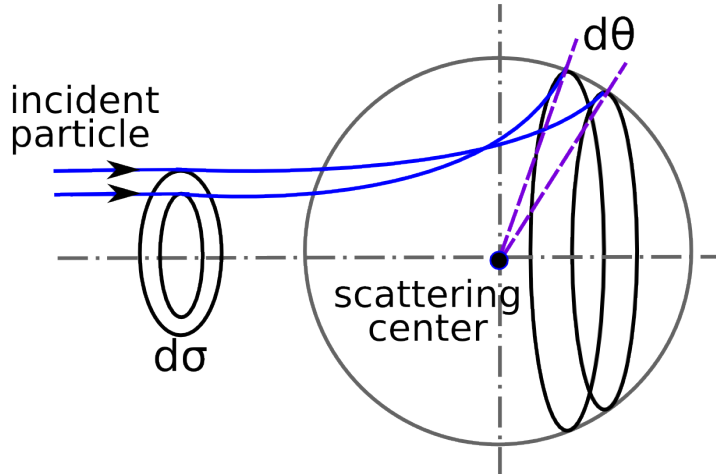
479 In this dissertation, we study an electroweak process $W\gamma \rightarrow l\nu_l\gamma$, more specifically, probe
480 TGC vertex $WW\gamma$ (Eq. 22). To do that, we are measuring a differential cross section with
481 respect to the photon transverse momentum. The concept of the cross section in particle physics
482 is discussed in the next chapter.

483

484 2.2 Cross Section and Luminosity

485 In this dissertation we are measuring the total and the differential cross section. The cross section
 486 in particle physics is the interaction probability per unit flux of incident particles [12]. It can
 487 be interpreted as area which must be crossed by an incident particle in order to interact with
 488 a scattering center, or, in case of a differential cross section, area $d\sigma$ within which an incident
 489 particle must appear to be scattered off by an angle $d\theta$ (Fig. 8). The relationship between $d\sigma$
 490 and $d\theta$ gives us the expression for a differential cross section $d\sigma/d\theta$. Integrating over $d\theta$, one
 491 would get the total cross section σ .

492 In Fig. 8 an incident particle is the same as a final state particle, however in particle physics
 493 final state particles can differ from initial state particles, and we measure a differential cross
 494 section with respect to a parameter X of the final state particle. Differentiating σ by X we get
 495 the expression for the differential cross section $d\sigma/dX$.



501 Figure 8: Illustration of the differential cross section concept in the classical case.

502 Referring to the Fig. 8, a number of particles passing through the area σ per unit time is
 503 $N = L \cdot \sigma$, where L is the flux of incident particles and is called luminosity. Therefore, the cross
 500 section σ of a specific process can be determined from an experiment as $\sigma = N/L$.

504 A cross section also can be computed theoretically. The formula to compute a cross section is:
 505

$$\sigma = \frac{W_{fi}}{L} N_{fs}, \quad (29)$$

506 where W_{fi} is a transition probability between final and initial states of the system per unit
 507 volume, L is the flux of initial particles, and N_{fs} is the density of final states [8], Ch. 4.3.

508 The formula of the cross section is called the Fermi's Golden Rule [1]. In case of the scattering
 509 of two particles to three final state particles $1 + 2 \rightarrow 3 + 4 + 5$, it takes the following form:

$$\sigma = \frac{1}{4\sqrt{(p_1 p_2)^2 - (m_1 m_2)^2}} \int |M|^2 (2\pi)^4 \delta^4(p_1 + p_2 - p_3 - p_4 - p_5) \prod_{j=3}^5 \frac{1}{2\sqrt{\bar{p}_j^2 + m_j^2}} \frac{d^3 \bar{p}_j}{(2\pi)^3}, \quad (30)$$

510 where p_i are 4-momenta and \bar{p}_i are three momenta of the initial state and the final state
511 particles, m_i are masses of particles, M is the process amplitude determined by the dynamics
512 of the particles interaction. All available momenta of the final state particles is called the phase
513 space.

514

515 The cross section of the hard scattering in proton-proton collisions $pp \rightarrow X + Y$ has two
516 ingridients: PDFs and a partonic cross section $\sigma_{ab \rightarrow X}$. The partonic cross section is described
517 by perturbative QCD while PDFs require non-perturbative computations and are determined,
518 in part, from experiments (Fig. 7). According to the QCD factorization theorem [9]:

519

$$\sigma(pp \rightarrow X + Y) = \sum_{a,b} \int dx_a dx_b f_a(x_a, Q^2) f_b(x_b, Q^2) \sigma(ab \rightarrow X). \quad (31)$$

520 In case of $W\gamma$ process, X is $l\nu\gamma$, ab are $q_i\bar{q}_j$ or $q_j\bar{q}_i$. Q^2 is the large momentum scale that char-
521 acterizes hard scattering, f_a and f_b are PDFs, x_a and x_b are fractions of momenta of the partons.

522

2.3 Standard Model $W\gamma$ Production

A W boson in proton-proton collisions can be produced in the processes $q\bar{q}' \rightarrow W$ where q and \bar{q}' are a quark and an antiquark which have a total charge of +1 if producing a W^+ boson or of -1 if producing a W^- boson. The processes $u\bar{d} \rightarrow W^+$ and $d\bar{u} \rightarrow W^-$ are the most likely to occur because u and d are valence quarks in a proton. Antiquarks \bar{d} and \bar{u} come from sea $q\bar{q}$ pairs of the other proton.

A W boson decays immediately after being created, and we do not detect the W boson itself but its decay products. Decay modes of a W boson include $W^\pm \rightarrow l^\pm \nu_l (\bar{\nu}_l)$ where $l^\pm = e^\pm, \mu^\pm$ or τ^\pm with branching fractions of 11% per a leptonic channel [5]. The rest 67% stands for various $W \rightarrow q\bar{q}'$ decays. In this dissertation we only consider $W^\pm \rightarrow \mu^\pm \nu_\mu (\bar{\nu}_\mu)$ and $W^\pm \rightarrow e^\pm \nu_e (\bar{\nu}_e)$ as the cleanest channels.

A photon can be emitted from any charged particle of the process: a quark, an antiquark, a charged lepton or a W boson (Fig. 9, top). A quark and an antiquark are initial state particles and, therefore, if one of them radiates a photon, we call such process the Initial State Radiation (ISR). A muon or an electron is a final state particle and if it radiates a photon, we call such process the Final State Radiation (FSR). Finally, a W boson is a gauge boson and if it radiates a photon, the process has a vertex with three gauge bosons: $WW\gamma$, and we call such process the Triple Gauge Coupling (TGC).

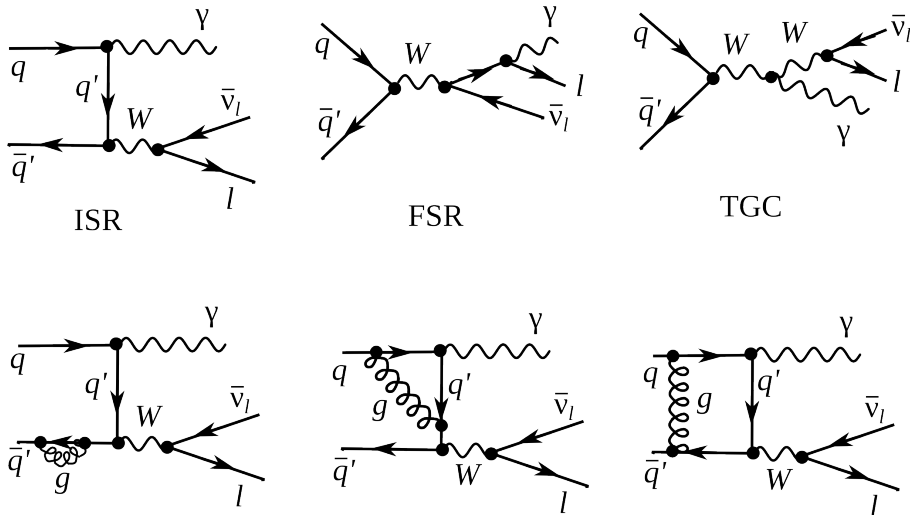


Figure 9: Feynman diagrams of $W\gamma$ production

The electroweak Lagrangian is described in Chapter 2.1. It is possible to derive equations of motion from the Lagrangian for any fields involved [1]. However, in a quantum field theory equations of motion cannot be solved exactly and, therefore, the perturbative approach is used if coupling constants are $g \ll 1$.

To represent the process graphically Feynman diagrams were invented. Also the diagrams can be used to calculate the process amplitude M from Eq. 30 because they are determined by Lagrangian terms relevant to the process. There is infinite number of Feynman diagrams corresponding to any specific process and the total amplitude of the process is a sum of individual amplitudes of each diagram and it is not technically possible to take into account all of them.

554 The perturbative approach arranges all the diagrams by orders of contribution because each
555 vertex is assigned a coupling constant and, therefore, the Feynman diagrams with fewer vertices
556 would give a significantly larger contribution to the amplitude. In Fig. 9 we have examples of the
557 Leading Order (LO) and the Next-to-Leading Order (NLO) Feynman diagrams (top and bottom
558 diagrams respectively).

559

560 The $W\gamma$ process is represented by four LO Feynman diagrams with three vertices each. The
561 $W\gamma$ process amplitude and cross section are long, complicated expressions, therefore, they are not
562 quoted in this dissertation. The first calculation of the $W\gamma$ process with necessary formulas can
563 be found in [14].

564

565 The NLO corrections shown in Fig. 9 are QCD corrections only which include gluon loops
566 at the same quark line and exchange of a gluon between two different quark lines however QED
567 and weak NLO diagrams are also possible. QED corrections mean radiations of extra photons
568 by charged particles, exchange of photons between different charged particles or a photon can be
569 radiated and absorbed by the same charged particle forming a loop. Similarly, weak corrections
570 mean extra virtual W or Z bosons. But the QCD corrections are the largest.

571

572 The theoretical cross section in particle physics is important not only for analyzing the measurement
573 result but also for producing the simulation which is then actively used while performing the measurement.
574 The simulation consists of two parts: the generation of the process and the simulation of the particles paths through the detector. While the second one depends on the
575 well-known properties of the particles and the detector configurations, the first part relies on the
576 theory.

577

578 The most precise theoretical $W\gamma$ cross section available is the Next-to-Next-to-Leading Order
579 (NNLO) cross section in QCD [15]. The effect of the NNLO correction ranges from 19% to 26%
580 compared to the NLO cross section depending on the selection conditions. The contributions
581 from the higher order corrections is estimated to be $\pm 4\%$. However, the NNLO theoretical result
582 was published in 2015 only and there is still no simulation available based on that result. The
583 simulation used in this analysis is LO + up to two hadronic jets simulation which found to give
584 the same predictions as the NLO result.

585

586 In addition to the SM predictions, there are certain BSM theories which predict an enhancement
587 of the contribution from the TGC diagram. The discussion of these BSM effects and how
588 they affect the $W\gamma$ process takes place in Chapter 2.4.

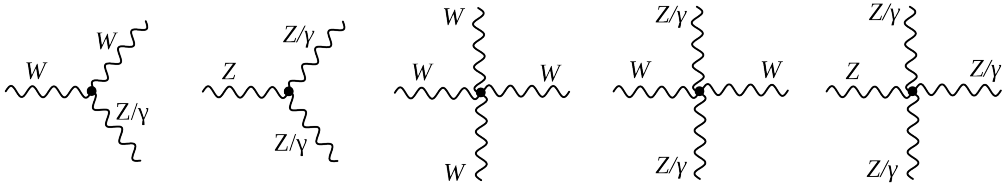
589

591 2.4 Anomalous $W\gamma$ Production

592 Most BSM physics theories predict the existence of particles which are heavier than the discov-
 593 ered energy range. If their masses are not accessible even by the most energetic machines, the
 594 direct detection of such particles is not possible. However, they can contribute to the productions
 595 of lower energetic particles producing loops where such heavy particles would be off-shell. The
 596 loops would give additional contributions to the process amplitude and, therefore, there would
 597 be more events produced in the process than one can expect based on the SM predictions.

598 These effects can be probed by precision measurements of the SM processes. In the elec-
 599 troweak sector processes of such interest include diboson and triboson productions which can
 600 occur through triple gauge couplings and quartic gauge couplings.

601 Triple and quartic gauge couplings (QGC) are represented by vertices with three and four
 602 bosons (Fig. 10). As discussed in Chapter 2.1, charged TGC and QGC are possible at tree level
 603 in the SM while neutral TGC and QGC are not.



606 Figure 10: TGC and QGC vertices

607 To account for the effects from the potential loops of heavy particles, we introduce an ef-
 608 fective Lagrangian with arbitrary values of coupling constants which can be shrunk to the SM
 609 Lagrangian if these constants would have their SM values. Such approach makes our searches
 610 model-independent because we do not specify which exactly particles form the loops but instead
 611 just check whether there is a deviation from the SM.

612 In $W\gamma$ measurement we can probe $WW\gamma$ vertex only. The most general Lorentz invariant
 613 Lagrangian of this vertex takes the following form [17]:

$$615 iL_{eff}^{WW\gamma} = iL_{eff(1)}^{WW\gamma} + iL_{eff(2)}^{WW\gamma} + iL_{eff(3)}^{WW\gamma} \quad (32)$$

$$iL_{eff(1)}^{WW\gamma} = e[g_1^\gamma A^\mu (W_{\mu\nu}^- W^{+\nu} - W_{\mu\nu}^+ W^{-\nu}) + \kappa_\gamma W_\mu^+ W_\nu^- A^{\mu\nu} + \frac{\lambda_\gamma}{m_W^2} A^{\mu\nu} W_\nu^{+\rho} W_{\rho\mu}^-] \quad (33)$$

$$iL_{eff(2)}^{WW\gamma} = e[i g_5^\gamma \epsilon_{\mu\nu\rho\sigma} ((\partial^\rho W^{-\mu}) W^{+\nu} - W^{-\mu} (\partial^\rho W^{+\nu})) V^\sigma + i g_4^\gamma W_\mu^- W_\nu^+ (\partial^\mu A^\nu + \partial^\nu A^\mu)] \quad (34)$$

$$iL_{eff(3)}^{WW\gamma} = e[\frac{\tilde{\kappa}_\gamma}{2} W_\mu^- W_\nu^+ \epsilon^{\mu\nu\rho\sigma} A_{\rho\sigma} - \frac{\tilde{\lambda}_\gamma}{2m_W^2} W_{\rho\mu}^- W_\nu^{+\mu} \epsilon^{\nu\rho\alpha\beta} A_{\alpha\beta}] \quad (35)$$

616 where e is the absolute value of the electron charge, A^μ is the photon field, $W^{\pm\mu}$ are fields of
 617 W^\pm bosons, $W_{\mu\nu} = \partial_\mu W_\nu - \partial_\nu W_\mu$, $A_{\mu\nu} = \partial_\mu A_\nu - \partial_\nu A_\mu$, m_W is the mass of a W boson, g_1^γ , κ_γ ,
 618 λ_γ , g_5^γ , g_4^γ , $\tilde{\kappa}_\gamma$, and $\tilde{\lambda}_\gamma$ are constants.

619

620 Despite there are 7 constants in the extended Lagrangian, only λ_γ and κ_γ are considered
 621 in the aTGC searches. The rest of the constants are fixed to their SM values based on various
 622 considerations. Thus, $g_1^\gamma = 1$ and $g_5^\gamma = 0$ are fixed to obey the electromagnetic gauge invariance
 623 for the on-shell photons. The non-zero value of g_5^γ also violates C and P conservations, and
 624 non-zero values of g_4^γ , κ_γ , λ_γ violate the CP conservation law. Such violation parametrizations
 625 are not considered in charged TGC measurements now but might get considered in the future.

626 The presence of aTGC would have larger effects at high energy scales. Fig. 11 shows these
 627 effect in P_T^γ spectrum of 7 TeV $W\gamma \rightarrow \mu\nu\gamma$ measurement. Fig. 12 shows the examples of these
 628 effects in m_{ll} spectrum in 8 TeV $WW \rightarrow l\bar{l}l\nu$ measurement (left) and P_T^γ spectrum in 7 TeV
 629 $Z\gamma \rightarrow \nu\nu\gamma$ measurement (right). It is seen on the plots that aTGC spectrum at low m_{ll} or low
 630 P_T^γ coincides with the SM prediction but for higher m_{ll} or P_T^γ the disagreement becomes more
 631 significant.
 632

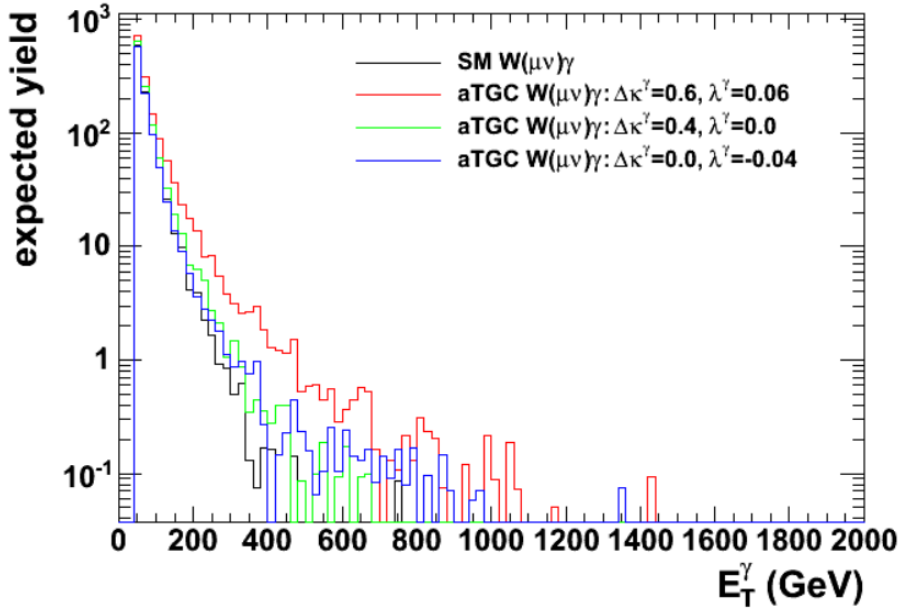


Figure 11: Distributions of P_T^γ of simulated $W\gamma \rightarrow \mu\nu\gamma$ events with different values of aTGC constants at LHC energy of $\sqrt{s} = 7$ TeV. Source of figure: [18].

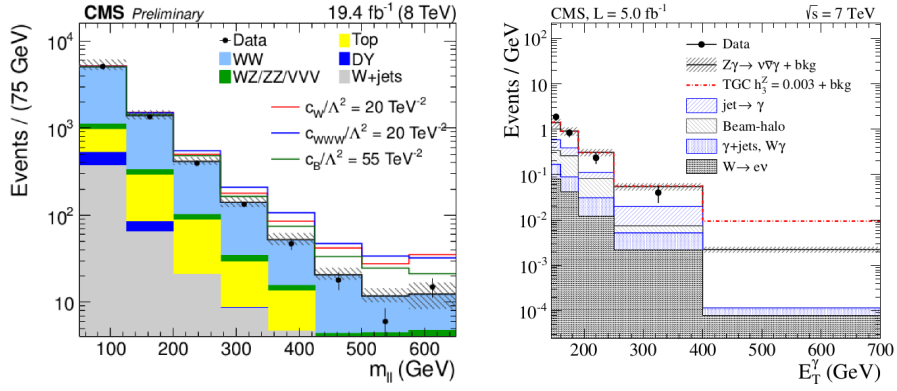


Figure 12: Examples of the potential effects of non-zero TGC constants in m_{ll} spectrum in 8 TeV $WW \rightarrow l\nu l\nu$ measurement (left) [29] and P_T^γ spectrum in 7 TeV $Z\gamma \rightarrow \nu\nu\gamma$ measurement (right) [30].

2.5 Measurements in the Past

ATGC parameters of $WW\gamma$ vertex can be probed in $W\gamma$, WW , and WZ measurements. Limits on $\Delta\kappa_\gamma$ and λ_γ constants from different D0 [19], LEP [20], ATLAS [21], [22], [23] and CMS [25], [26], [27], [28] measurements are summarized in Fig. 13.

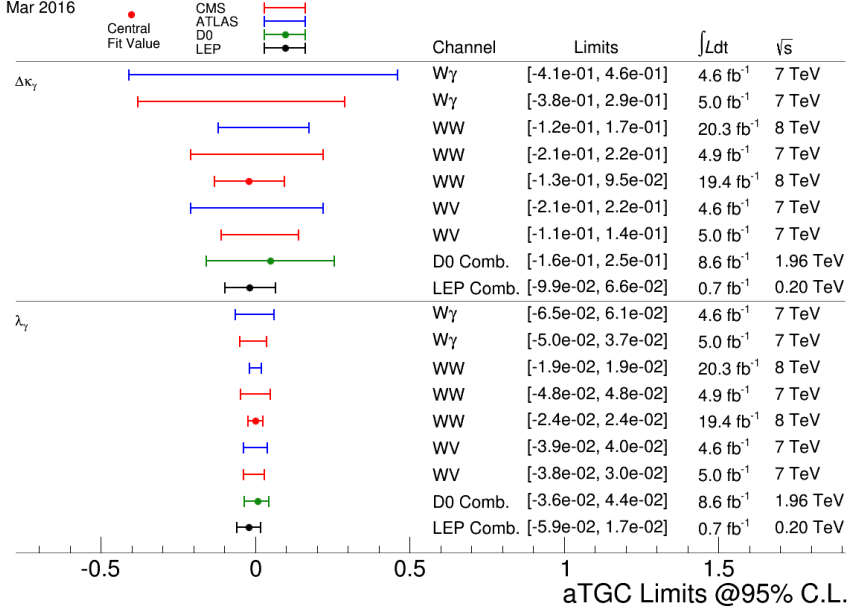


Figure 13: Summary of limits on the $WW\gamma$ aTGC coupling constants. Figure from [24]

The most recent measurements of $W\gamma$ production were performed by CMS [25] and ATLAS [21] collaborations with pp collisions at $\sqrt{s} = 7 \text{ GeV}$ collected in 2011. The measurements are based on 5 fb^{-1} and 4.6 fb^{-1} of integrated luminosity with CMS and ATLAS respectively. Both collaborations considered two channels: $W\gamma \rightarrow \mu\nu\gamma$ and $W\gamma \rightarrow e\nu\gamma$.

Dibosons processes are rare in pp -collisions and we have to filter out events of our interest from many processes which are more likely to happen. To do that, we apply variety of selection criteria which reject most of background events increasing our signal rate as much as possible. However, even after we applied all possible selection criteria, majority of our selected events are still background events and it is not possible to reduce the background any further without also significantly reducing signal.

The major source of such irreducible background is the fake photon background where hadronic jets are misidentified as photons. Such events originate from $W+\text{jets}$ process mostly but $Z+\text{jets}$ and $t\bar{t}+\text{jets}$ events contribute to this source of the background as well. The second major background for the electron channel is the fake photon background where electron can be misidentified as a photon. Such events are coming from $Z+\text{jets}$ events. Other sources of backgrounds include real- γ backgrounds, fake lepton + real photon and fake lepton + fake photon sources.

Both channels provide measurements of p_T^γ spectra because this variable is the most sensitive to the potential ATGC. The p_T^γ spectra of the selected events in data superimposed with selected events in the simulation of the signal and estimated background contribution for the muon and electron channels are shown in Fig. 14 for CMS and in Fig. 15 for ATLAS. Both measurements show a good agreement.

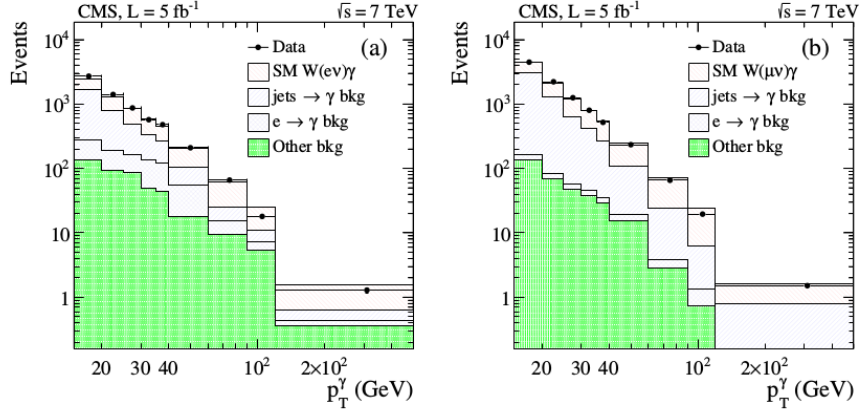


Figure 14: The distribution fo the p_T^γ of $W\gamma$ candidates in the analysis of 7 TeV CMS data. Data vs signal MC + background estimates. Left: $W\gamma \rightarrow e\nu\gamma$, right: $W\gamma \rightarrow \mu\nu\gamma$ [25].

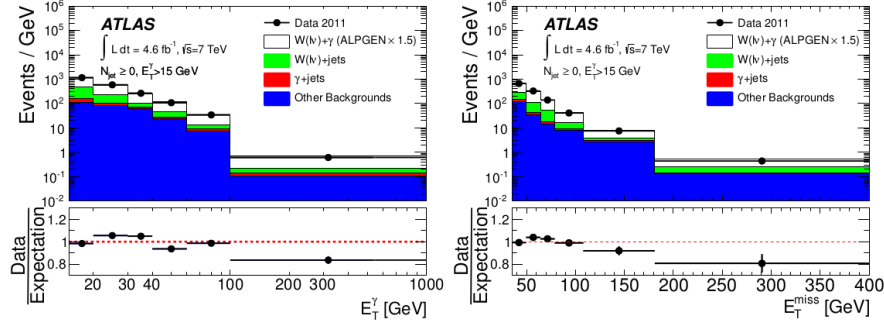


Figure 15: The distribution fo the p_T^γ (left) and E_T^γ (right) of $W\gamma$ candidates in the analysis of 7 TeV ATLAS data. Data vs signal MC + background estimates [21].

CMS provides measurements of the P_T^γ spectrum, the total cross section within the phase spaces of $\Delta R > 0.7$, $P_T^\gamma > 15$ GeV, $P_T^\gamma > 60$ GeV and $P_T^\gamma > 90$ GeV, and limits on aTGC coupling constants. The phase space restrictions come from the considerations of the detector acceptance, reducing heavily background-dominated regions and theory.

ATLAS, in addition to the P_T^γ spectrum, total cross section and limits, provides the differential cross section and cross section with different number of associated jets. No evidence of a new physics is observed.

In this dissertation we are measuring total and differential $d\sigma/dP_T^\gamma$ cross section however we do not derive limits on aTGC coupling constants. The measurement details and results are available in Chapter 5.

678 **3 Experimental Setup**

679 3.1 Large Hadron Collider

680 The Large Hadron Collider (LHC) [31], [32], [33] is the largest particle accelerator and the most
681 ambitious research facility ever built. The LHC is placed into a tunnel originally built for the LEP
682 accelerator. The LEP was decommissioned to make room for the LHC. The tunnel is about 27 km
683 in circumference, located at the Swiss-French boundary up to 100 meters undergroud.

684 Before entering LHC, particle beams are going through several stages of the acceleration and
685 the LHC is the last element of the chain of the CERN's accelerator complex (Fig. 16). Protons
686 are extracted from hydrogen atoms, are accelerated by Linac2 to energies of 5 MeV, then injected
687 into the Proton Synchrotron Booster (PSB) where they reach energies of 1.4 GeV. After that
688 protons are sent to PS and Super PS (SPS) where they are accelerated up to 25 GeV and 450 GeV
689 respectively. Finally, protons enter the LHC and are accelerated to reach their collision energies
690 of several TeV per beam. Besides protons, the complex also accelerates and collides lead ions
691 however in this dissertation we analyze data from proton-proton collisions only and, therefore,
692 are not discussing lead ion collisions.

693 Main goals of LHC were to detect the SM Higgs boson if it existed and to search for evidences
694 of BSM physics which may give a clue on understanding the phenomena including but not limited
695 to the dark matter, the matter-antimatter asymmetry, the nature of the gravitational force. Six
696 detectors are installed at the LHC to detect particles and perform the relevant measurements.
697 There are general purpose detectors ATLAS and CMS, there is LHCb which specializes of the
698 physics of B-mesons, and ALICE which is designed to detect products of heavy ion collisions. In
699 addition, there are two relatively small detectros: LHCf and TOTEM which are installed close
700 to the ATLAS and CMS collision points respectively.

701 A new particle with mass $m = 125$ GeV was discovered by the CMS [3] and the ATLAS [4]
702 collaborations in 2012. The particle is consistent with the SM Higgs boson predicted by the
703 EWK sector of the SM. The discovery of the Higgs boson is the greatest achievement by the
704 LHC to date.

705 While different BSM searches have been constituting a significant part of the LHC physics
706 program since the beginning of its operation, no deviations from the SM were found by any of
707 the experiments. The searches continue with higher beam energies and larger amount of data.

711 The design energy of the LHC is 7 TeV per beam however several lower energy points were
712 and are being probed. In 2010-2011 the LHC operated at energy of 3.5 TeV per beam which was
713 already higher than energy of any other collider. In 2012 the energy increased up to 4 GeV. In
714 2013-2014 the LHC was shut down for upgrades. Collisions were restarted at 6.5 TeV in 2015
715 and the LHC is still operating at this energy in 2016.

718 All important measurements performed at lower energies are also repeated at higher energies
719 because the ability to probe higher energy scales increases our chances for a discovery and even
720 if no deviations from the known physics are found at a given energy point, the discovery is still
721 possible to happen as we go higher in the energy.

723 In addition to the beam energy, there are many other collider parameters. A brief summary
724 of them is available in Tab. 2. One of the most important parameters of an accelerator is the
725 ability to produce a large number of interesting collisions which is determined by the luminosity.
726 The instantaneous luminosity is determined by the following expression [5]:

$$729 L = f \frac{n_1 n_2}{4\pi \sigma_x \sigma_y}$$

730 where n_1 and n_2 are numbers of particles in colliding bunches, f is a frequency of collisions,
731 σ_x and σ_y are beam sizes in horizontal and vertical directions. To determine the integrated
732 luminosity, one has to integrate the instantaneous luminosity over time:

734 $L_{int} = \int L dt$

735

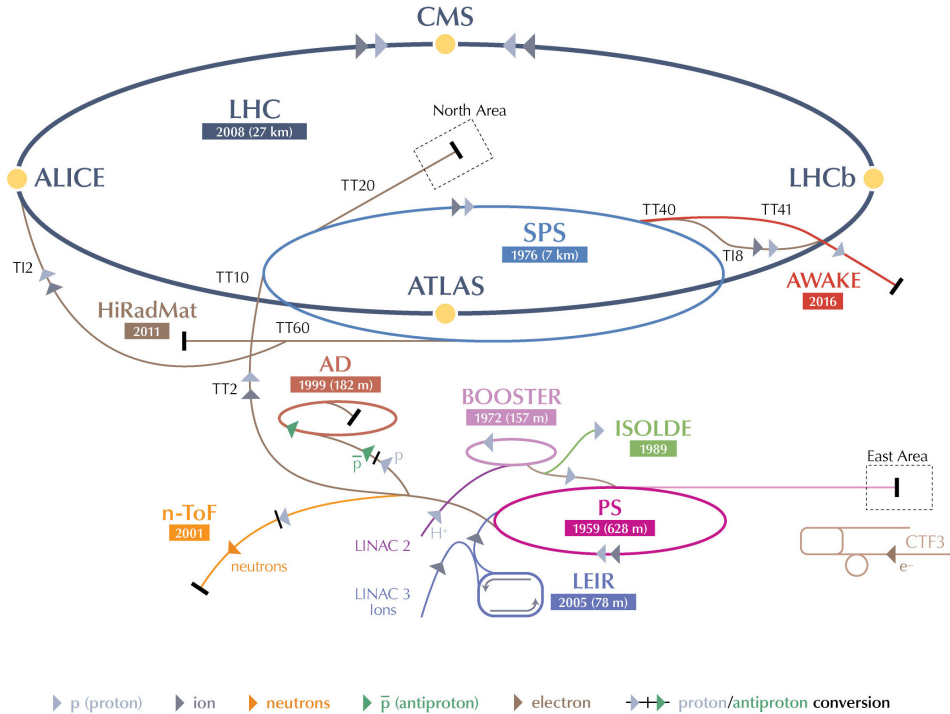
736 The luminosity of the LHC is also higher than of any previously existed collider. The integrated
 737 luminosity of the LHC for different years of the operation are shown in Fig. 17. Run periods of
 738 LHC in 2010-2012 refer to Run I of the LHC operation. While working on energy of $\sqrt{s} = 7$ TeV,
 739 LHC delivered 44.96 pb^{-1} and 6.1 fb^{-1} of data in 2010 and 2011 year respectively. In 2012 the
 740 working energy of LHC was $\sqrt{s} = 8$ TeV, and the integrated luminosity was $L_{int} = 23.3 \text{ fb}^{-1}$.
 741 After a long shutdown, LHC was upgraded for Run II, to operate on $\sqrt{s} = 13$ TeV in 2015 and
 742 delivered 4.22 fb^{-1} of data by the end of 2015. In 2016 LHC continues operation on $\sqrt{s} = 13$ TeV
 743 and by the end of September the integrated luminosity already exceeded a value of 30 fb^{-1} [37].
 744

745

746 The measurement of this dissertation is performed at the energy of 4 TeV per beam or at
 747 the center of mass energy $\sqrt{s} = 8$ TeV with 19.6 fb^{-1} of data. The same process was measured
 748 at $\sqrt{s} = 7$ TeV with about four times less amount of data by both CMS and ATLAS. These
 749 measurements are discussed in greater details in Ch. 2.5.

750

CERN's Accelerator Complex



LHC Large Hadron Collider SPS Super Proton Synchrotron PS Proton Synchrotron

AD Antiproton Decelerator CTF3 Clic Test Facility AWAKE Advanced WAKEfield Experiment ISOLDE Isotope Separator OnLine Dvice

LEIR Low Energy Ion Ring LINAC LINear ACcelerator n-ToF Neutrons Time Of Flight HiRadMat High-Radiation to Materials

© CERN2013

Figure 16: CERN's accelerator complex. Source of the figure: [34].

Table 2: Main parameters of LHC [31]

Circumference	27 km
Dipole operating temperature	1.9 K
Number of magnets	9593
Number of main dipoles	1232
Number of main quadrupoles	392
Number of RF cavities	8 per beam
Nominal energy, protons	7 TeV
Nominal energy, lead ions	2.76 TeV per nucleon
Peak magnetic dipole field	8.33 T
Min. distance between bunches	7 m
Design luminosity	$10^{34} \text{ cm}^{-2} \text{ s}^{-1}$
No. of bunches per proton beam	2808
No. of protons per bunch (at start)	1.1×10^{11}
No. of collisions per second	600 millions

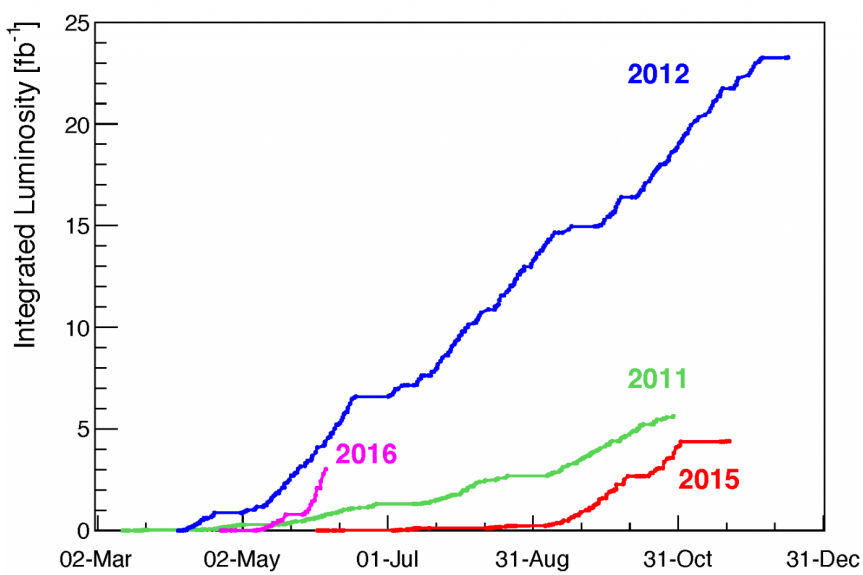


Figure 17: LHC integrated luminosity by year. Source of the figure: [35].

3.2 Compact Muon Solenoid

3.2.1 Introduction

The CMS is a general-purpose detector designed for detecting various highly energetic particles which are being produced in pp collisions at the LHC. The CMS has a broad program with goals of direct and indirect searches of the BSM physics including but not limited to supersymmetric particles. Its main feature is a huge magnet to create a magnetic field of 4T to curve charged particles in the tracking system and 2T outside to curve muons in the muon system.

The CMS detector is a cylindrically symmetric with a colliding beam as a central axis. Cartesian, cylindrical and spherical coordinates are all used to describe the CMS geometry, depending on the context. The x -axis of the CMS points towards the center of the LHC while the y -axis points vertically up. The direction of the z -axis corresponds to the counterclockwise direction of the LHC beam (Fig. 18, left). Cylindrical coordinates are defined as $r = \sqrt{x^2 + y^2}$, $\phi = \arctan(y/x)$. Instead of the polar angle θ , it is more convenient to use the pseudorapidity $\eta = -\ln \tan \theta/2$. A pseudorapidity changes from $\eta = -\infty$ to $\eta = +\infty$ for directions parallel to the beam axis with the value of $\eta = 0$ for a direction perpendicular to the beamlime. This variable is convenient for measurements because a distribution of a massless particle in η is nearly flat. The acceptance of the CMS in η is limited and varies from $|\eta| = 2.4$ to $|\eta| = 5.0$ depending on a subdetector.

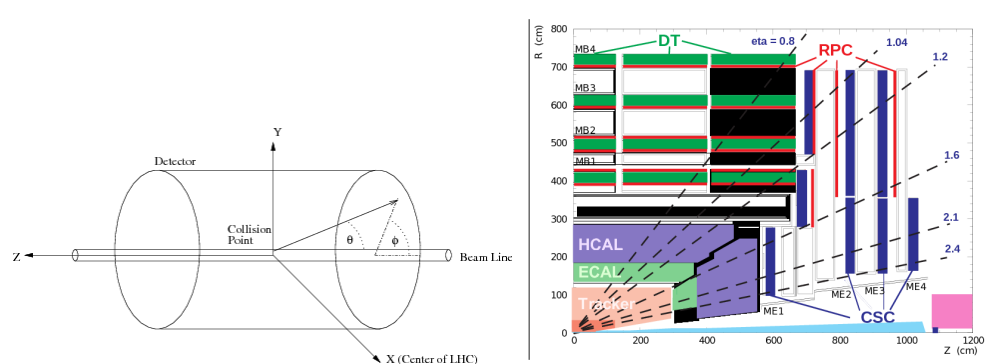


Figure 18: Left: CMS coordinate system. Right: pseudorapidity ranges for different CMS subdetectors.

The detector consists, from inner to outer layer, of a tracking system, an electromagnetic calorimeter (ECal), a hadronic calorimeter (HCal), a magnet and a muon system. Having the tracking system, ECal and HCal inside of a large solenoid makes the detector compact. A segment of a CMS slice in $r - \phi$ plane is shown in Fig. 19.

When a heavy particle is produced in a collision, it decays immediately, and we detect its long-living decay products including an electron, a photon, a muon, a neutral hadron or a charged hadron. Depending on the trace left by a particle in different subdetectors we can identify a particle. Electrons and positrons leave curved tracks in the tracking system and then induce showers in the electromagnetic calorimeter (ECal). Photons induce the same electromagnetic showers in ECal however, as neutral particles, they do not leave tracks in the tracking system. Hadrons normally travel through the ECal undisturbed and induce a hadronic shower in the hadronic calorimeter (HCal). Charged and neutral hadrons can be distinguished from each other by checking whether they leave a track in the tracking system or not. Muons are the only particles which penetrate through the ECal, the HCal and the magnet and leave tracks in the CMS muon system. Neutrinos are not detected by CMS.

787

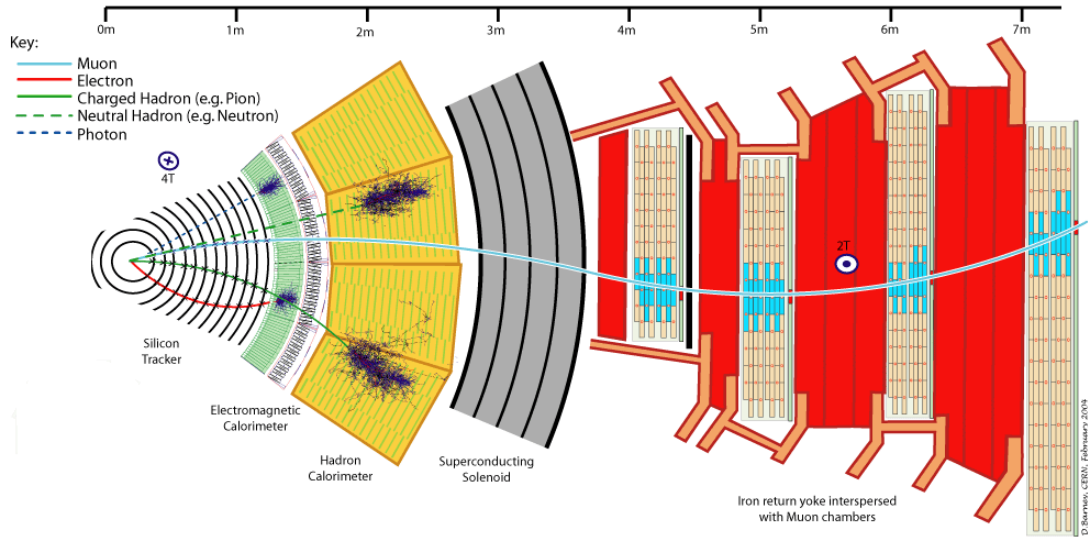


Figure 19: CMS slice.

788 All subdetectors are important for the $W\gamma$ measurement and the remainder of this chapter
 789 describes the subdetectors in greater details. Muons and electrons which we have as final state
 790 particles are both affected by CMS magnetic field allowing the tracking system and the muon
 791 system to measure their trajectory parameters and momenta. In this dissertation we use the
 792 information of the primary vertex determined by the tracking system to select our events. Also
 793 the tracker provide us the information about electrons trajectories and momenta in the electron
 794 channel and distinguishes between electrons and photons.
 795

796 3.2.2 Magnet

797 A magnetic field in a particle detector is necessary to measure momenta of charged particles
 798 by track curvatures. The higher the momentum is, the less a particles's path is affected by the
 799 magnetic field. In CMS it is done in the tracking system for all charged particles and in the
 800 muon system for muons.
 801

802 The CMS magnet is placed between layers of HCal and a muon system. It creates a magnetic
 803 field of 4T inside the magnet, for the tracking system, and 2T outside the magnet, for the muon
 804 system. It is necessary to have stronger field in the tracking system because a density of tracks
 805 is much higher there than in the muon system and also the tracking system is much smaller and,
 806 therefore, more significant curvature is necessary to measure the momentum with high precision.
 807

808 The magnet is made of superconducting wires. An electric current flowing in the wires creates
 809 a uniform field inside the solenoid and also provides a magnetic field of a certain configuration
 810 outside the solenoid.
 811

812 3.2.3 Tracking System

813 The tracking system measures track geometry including particles trajectories and locations of
 814 primary and secondary vertices and momenta of charged particles. It needs to disturb particles

as little as possible so that they can pass through. Therefore, just a few measurements must be enough to reconstruct the track. The accuracy of a measurement of each hit is $10 \mu\text{m}$.

The tracking system consists of silicon pixels and silicon strips (Fig. 20). Collision tracks start at the center and then cross the layers of the tracking system. Tracks are straight in $r - z$ plane and curved by the magnetic field in the $r - \phi$ plane. The acceptance of the tracker system in $r - z$ plane is geometrically limited by $\eta = 2.5$ ($\eta = -\ln[\tan \theta/2]$, where θ is a polar angle).

The pixel tracker is the closest subsystem of CMS to the collision point thus it experiences the largest particle flux: at 8 cm from the collision point the flux is about 10 million $1/(\text{cm}^2\text{s})$, and the pixel detector with its 65 millions sensors is capable to reconstruct all these tracks. It consists of three layers of cylinders in the barrel with radii of 4 cm, 7 cm and 11 cm and four disks in the endcap, two disks at each side. The tracker is designed in such a way that a single track hits multiple sensors. Then the trajectory is reconstructed based on how much charge is collected on each sensor. This allows us to reach a spacial resolution of 15-20 μm which is much smaller than a distance between sensors.

The strip tracker is placed right after the pixel tracker and occupies the detector volume up to 130 cm around the beam axis. The strip tracker consists of four parts: the tracker inner barrel (TIB), the tracker inner disks (TID), the tracker outer barrel (TOB) and the tracker endcap (TEC) as shown in Fig. 20. In the strip tracker there are over 15,000 sensitive modules with a total number of 10 million strips. Each sensitive module consists of a set of sensors, its support structure and readout elements.

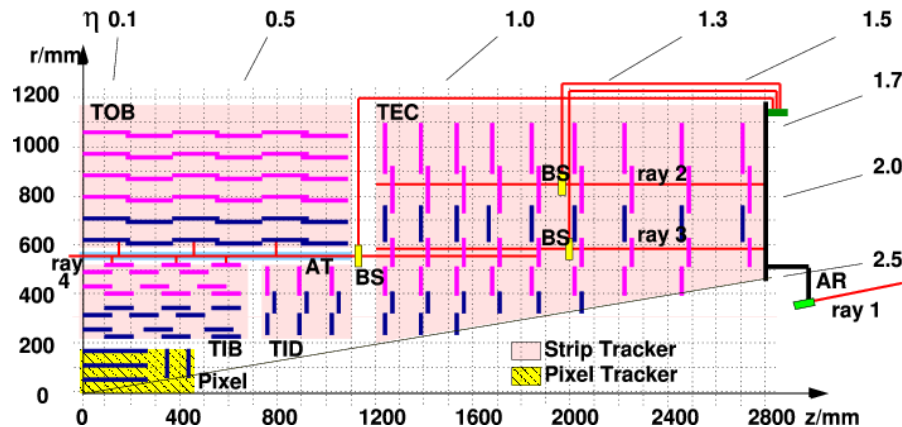


Figure 20: Slice of the CMS tracking system in $r - z$ plane.

3.2.4 Electromagnetic Calorimeter

The ECal measures energy of electrons and photons and also measures geometries of their trajectories. Electrons and photons interact with the ECal substance by inducing electromagnetic showers. Traces left by photons and electrons in the ECal are the same. To distinguish between these two particles, it is necessary to perform matching to the track in the tracking system. If there is a track, then there is an electron (or positron). If there is no track, then the particle is a photon.

The Ecal is a layer between the tracking system and the HCal. It is made of high-density lead tungstate crystals arranged in a barrel section and two endcap sections. The crystals work as scintillators. When electrons and photons pass through it, it produces light proportional to the

850 particle's energy. The scintillated light then is amplified by photomultipliers producing signals
851 on sensitive elements.

852 It is important for the Ecal to be able to distinguish between high energetic photons and
853 pairs of lower energetic photons e.g. from a π^0 decay. It is especially difficult in the endcap
854 sections where angle between two photon trajectories is small. Ecal preshower located in front
855 of the endcaps which have much smaller granularity provide extra spacial precision. Their strips
856 are 2 mm wide compared to 3 cm wide crystals in the main volume of the ECal.
857

858

859 **3.2.5 Hadron Calorimeter**

860 The HCal is placed right after the ECal and is the last subdetector within the magnet. The
861 HCal measures energies of charged and neutral hadrons. In addition, the HCal determines the
862 track parameters. Match to the tracking system has to be done: if a matching track found, then
863 it is a charged hadron otherwise it is a neutral hadron.

864

865 The HCal consists of alternate layers of absorbers and scintillators. Hadrons hit brass or steel
866 plate of absorber producing secondary particles. When emerge into the scintillator, the particles
867 induce hadronic and electromagnetic showers and emit blue-violet light which is further shifted
868 to the green region and read out by special boxes within the HCal. The secondary hadrons pro-
869 duced during the interaction with the absorber interact with the next absorber producing more
870 showers in the next layers of scintillators and also affect the total energy deposit. All hadrons
871 must be stopped inside the layers of the HCal.

872

873 **3.2.6 Muon System**

874 Muons pass through the ECal, the HCal and the magnet without interacting. They are the only
875 particles which are registered in the muon system which is placed outside the magnet and which
876 is the largest part of CMS detector.

877

878 There are four concentric layers of muon detectors (stations) and iron return yoke between
879 them. Muons induce several hits in the muon stations which are later fitted and matched to the
880 tracking system measurements to provide the best possible resolution in the measurements of all
881 parameters of the muon's trajectory and momentum.

882

883 There are three types of muon chambers used in the CMS muon system: drift tubes (DTs),
884 cathode strip chambers (CSCs) and resistive plate chambers (RPCs). Overall, there are 1400
885 muon chambers including 250 DTs, 540 CSCs and 610 RPCs.

886

887 The system of DTs measures positions of muons in the barrel. Each DT chamber is about 2 m
888 by 2.5 m in size. It consists of 12 layers of aluminium which are grouped by four. There are up
889 to 60 drift tubes in a layer. The middle group of layers measures z -coordinate and two other
890 groups determine the perpendicular coordinate.

891

892 Each drift tube is 4 cm in width, is filled with a gas and has a wire inside. When a charged
893 particle passes through the volume, it ionizes atoms and the wire receives an electric charge.

894

895 CSCs are placed in endcap regions. CSCs are arrays of anode wires which are crossed by
896 copper cathode strips placed in a gas volume. When a charged particle penetrates to the gas
897 volume, it ionizes the gas. Electrons drift to the wires while ions move to the strips. Strips are
898 perpendicular to wires, thus, we measure two coordinates for each particle.

899

900 RPCs are parallel capacitors made of high-resistivity plastic plates with a space between
901 them filled with a gas. RPCs provide quick measurements of muon momenta and are used for

902 triggering.

903

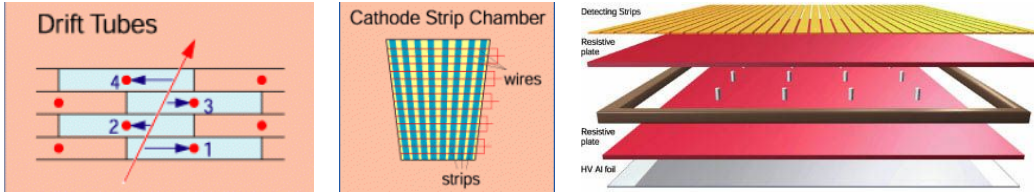


Figure 21: Components of the CMS muon system. Left to right: drift tubes, cathode strip chambers (CSCs), resistive plate chambers (RPCs).

904 **3.2.7 Triggering and Data Aquisition**

905 At peak luminosity, CMS experiences one billion proton-proton collisions per second which come
906 in bunches separated just by 25 ns from one other. New events come before the events from
907 the previous bunch crossing left the detector. To process the information from many different
908 collisions at the same time, data is stored in pipelines.

909

910 It is not technically possible to readout all these events. Moreover, we do not need most
911 of these events for a physics analysis because most of these events do not have a potential to
912 discover a new physics. We have resources to store about one hundred events out of one billion
913 that is why we need a trigger system which quickly decides what the best one hundred events are.

914

915 If the triggers were too loose, and we would select one hundred events too quickly, e.g., out
916 of a hundred million events, then CMS would not be able to process the rest 90% of events in a
917 givem set of one billion and we would lose 90% of potentially interesting events.

918

919 If the triggers were too strict, we would select, e.g, ten events out of one billion, not one
920 hundred and lose CMS potential to store and process data by 90% which would significantly
921 reduce our chances for a discovery.

922

923 Thus, the challenge of the trigger system is to select the best one hundred events out of one
924 billion and do that fast to be able to process every single event. To achive this goal, a two-level
925 trigger system was developed consisting from the Level 1 (L1) trigger and the high level trigger
926 (HLT) as shown in Fig. 22.

927

928 L1 is a hardware based trigger (Fig. 23). It uses information from the ECal, HCal and muon
929 system. L1 reduces frequency of coming events from 40 MHz to 100 kHz. Events which did not
930 pass the L1 trigger are lost forever while events which pass the L1 trigger are temporarily stored
931 to get checked by the HLT.

932

933 HLT is a software-based trigger. It uses information from all subdetectors and runs quick
934 reconstruction and identification algorithms to determine types of particles and their kinematics.
935 It reduces the number of events to 100 Hz. Events which did not pass HLT are lost forever.
936 Events which pass HLT are arranged into appropriate datasets depending on HLT selection cri-
937 teria they passed and stored for physics analyses.

938

939 **3.2.8 Event Reconstruction**

940 Where to place particle reconstruction, particle flow algorithm and MET? Check other theses

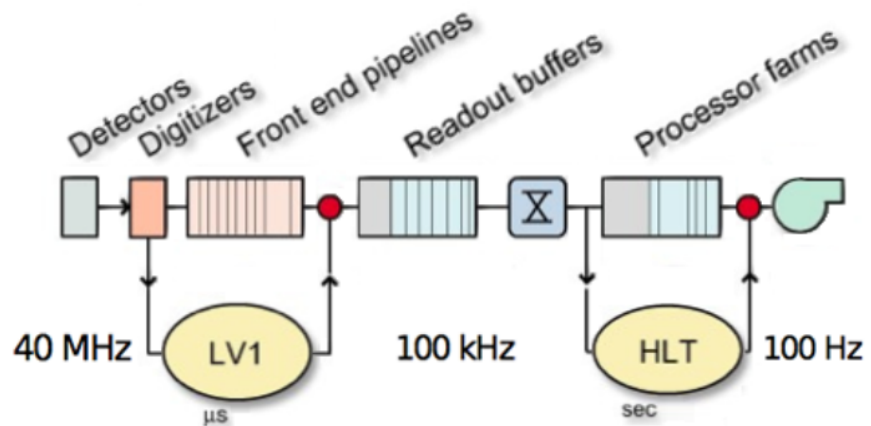


Figure 22: Two-level CMS trigger system.

941 Acceptance: particles which are too collinear and go to pipe; particles which get curved too
942 strongly

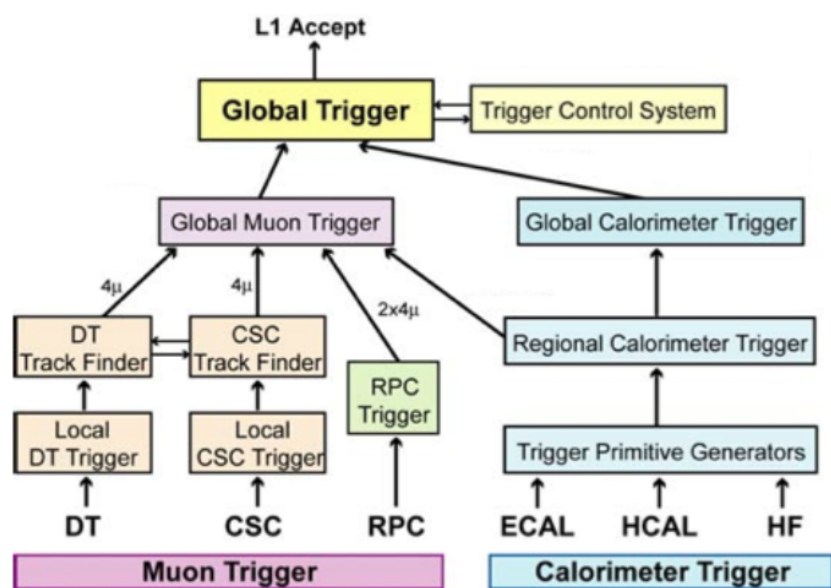


Figure 23: Level 1 CMS trigger system.

943 4 CMS Tracker Alignment

944 4.1 Algorithm

945 Why align?

946 How to align?

947 When align?

948 How to check that your alignment is good?

949
 950 A tracking system detects hits produced by a charged particle traveling through the detector.
 951 In a presence of a constant magnetic field the particle has a helical trajectory. A reconstruction
 952 algorithm determines the track parameters by fitting the positions of hits assuming the helix
 953 trajectory.

954
 955 Better hit resolution and the location uncertainty lead to better precision of a measurement
 956 of the track parameters. The location uncertainty depends on our knowledge of the positions and
 957 orientations in space of the tracking system modules. The hit resolution in the CMS pixel detector
 958 is $\sim 15 \mu\text{m}$. When the modules are mounted, their positions are known with precision of $\sim 200 \mu\text{m}$.
 959 Thus, we need to know positions of modules 20 times better than they are known when mounted.

960
 961 The procedure of the determination of the modules locations and orientations is called the
 962 tracker alignment. The concept of the track-based alignment can be illustrated in the example of
 963 the alignment of a toy tracker. When a charged particle passing through a detector (Fig. 24, top
 964 left) it crosses a toy tracker which consists of six flat equidistant modules (Fig. 24, top right). If
 965 the modules were placed exactly at their designed positions, we would observe the hits exactly at
 966 the points where the track crosses modules at the points of ideal geometry (Fig. 24, middle left).
 967 However, in a reality the positions and tilts of the modules are different from ones suggested by
 968 the ideal geometry (Fig. 24, middle right). Hits, indeed, are recorded at the places where mod-
 969 ules are actually mounted, not at the design ideal places (Fig. 24, bottom left). If we assumed a
 970 tracker to be ideal and a track to be smooth, we would see that our hits are off-track (Fig. 24,
 971 bottom right). So, we recalculate positions of the modules so that all the hits are laying on the
 972 same smooth track (Fig. 25, top left). But these recalculated positions still do not coincide with
 973 the actual positions (Fig. 25, top right). Then we record more and more tracks (Fig. 25, middle
 974 left and right). We take into account them all and determine the alignment parameters with
 975 necessary precision (Fig. 25, bottom left and right).

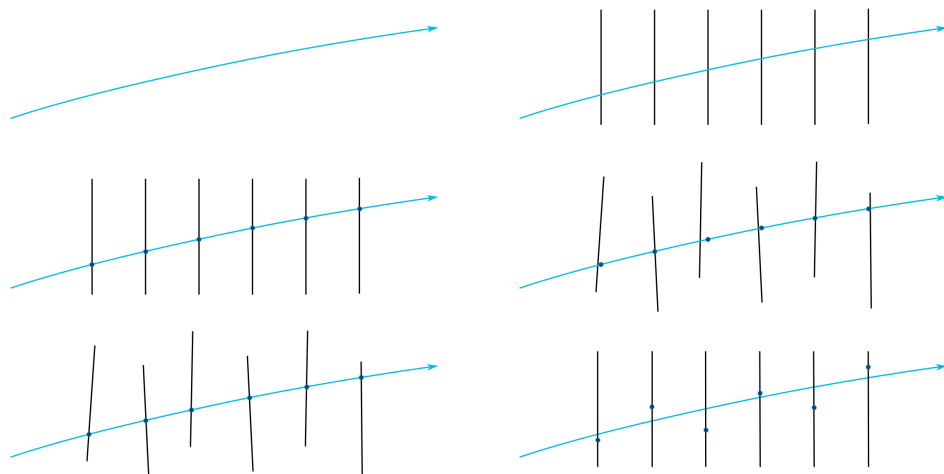


Figure 24: The alignment of a toy tracker, part 1.

977 When we record a track with a not-aligned tracker, we see that the track is not smooth. But

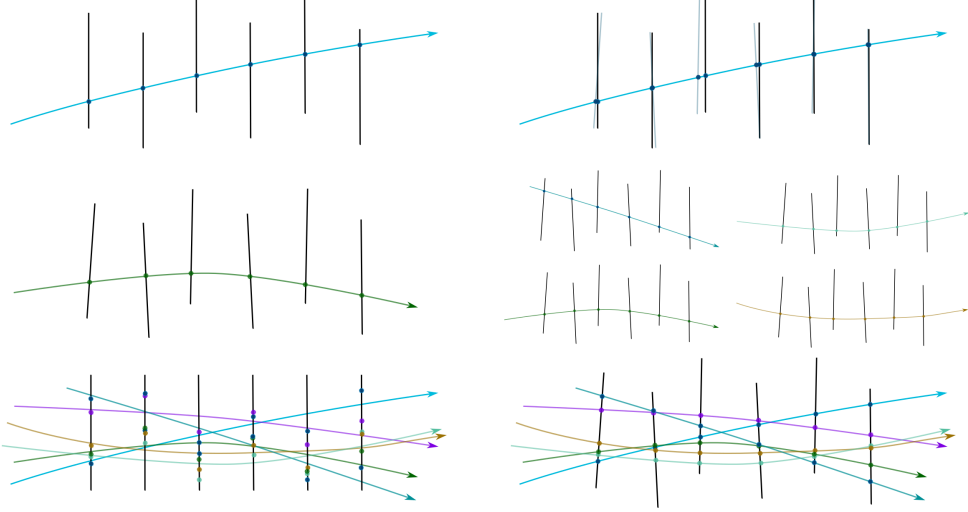


Figure 25: The alignment of a toy tracker, part 2.

978 that is because our knowledge of module positions is not exact. Thus, we can correct the positions
 979 assuming the track is smooth. But when we process the next track, we may find out that
 980 the positions have to be corrected again. Thus, we record many tracks and minimize residuals
 981 between measured and predicted hits.

982 The CMS tracker contains 1440 silicon pixel modules in PXB and PXF and 15148 silicon
 983 strip modules in TIB, TOB, TID, TEC.

985 The tracker alignment problem is the least squared problem. The expression to minimize is
 986 the following:

$$\chi^2(\mathbf{p}, \mathbf{q}) = \sum_j^{\text{tracks}} \sum_i^{\text{tracks}} \left(\frac{m_{ij} - f_{ij}(\mathbf{p}, \mathbf{q}_j)}{\sigma_{ij}} \right)^2 \quad (36)$$

989 where \mathbf{p} are parameters describing the tracker geometry, \mathbf{q}_j are parameters of the j^{th} track,
 990 $m_{ij} - f_{ij}$ are residuals, distances between the measured hit and a position predicted by the track
 991 fit, σ_{ij} is the Gaussian error of the measurement.

992 We can align the large substructures and individual modules with respect to their substructures.
 993 The parameters to align large substructures include their positions and orientations of the
 994 subdetectors (rotations). Thus, each subsystem is described by six parameters: three coordinates
 995 X, Y, Z and three angles α, β, γ . At the module level, we align positions and rotations with
 996 respect to the position s and angles of the corresponding large structure (Fig. 26). In addition,
 997 at the module level we align for surface deformations which are described by three parameters
 998 per sensor (Fig. 27).

1000 A track can be described with five parameters.

1002 We have two alignment algorithms: Millepede and HIP. Millededepe performs a simoultaneous fit
 1003 of all alignment parametes and all track parameters while HIP perform iterative fits of alignment
 1004 parameters \mathbf{p} and track parameters \mathbf{q}_j .

1005 It is important to use different sorts of tracks for the alignment. Cosmic tracks pass through
 1006 the detector vertically and do not allow us to connect different subdetectors to one another.

1008 Collision tracks originate from the collision point and go in all directions. However, those tracks
 1009 which cross TEC are all almost collinear and, therefore, it is difficult to measure z -coordinate of
 1010 TEC modules with collision tracks only.

1011

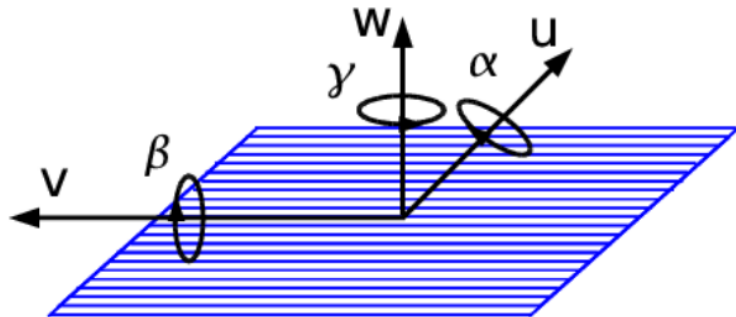


Figure 26: Alignment parameters.

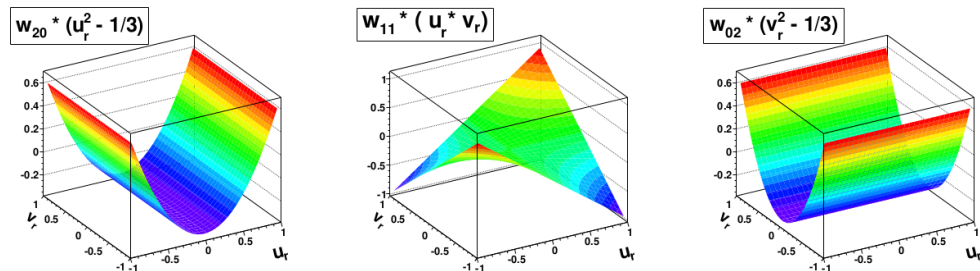


Figure 27: Surface deformations.

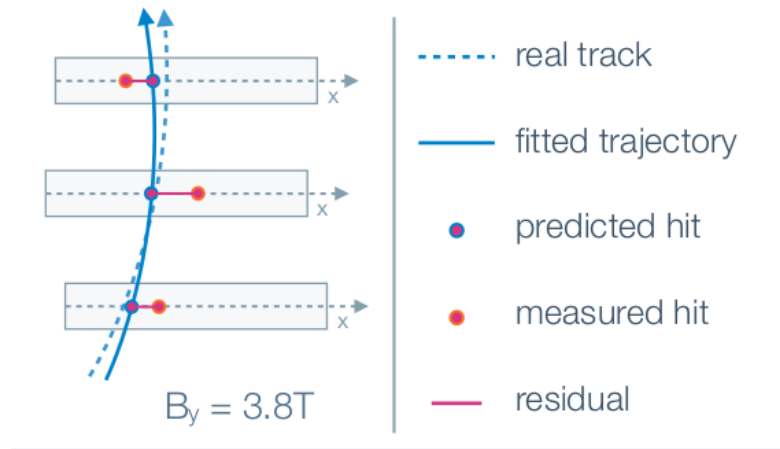


Figure 28: Track residuals.

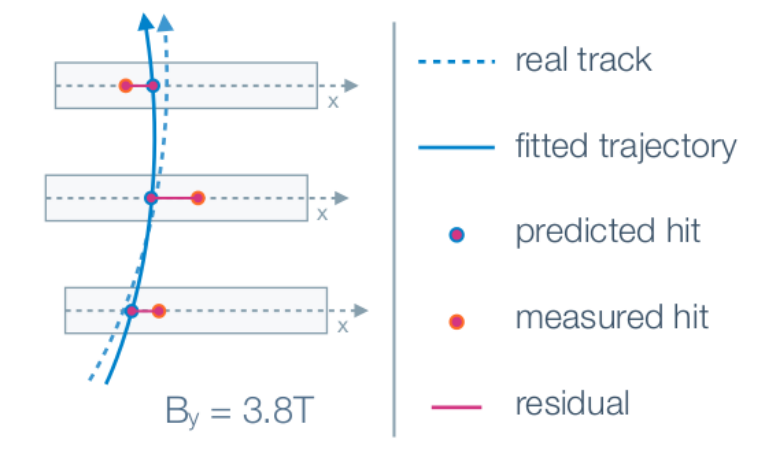


Figure 29: Track residuals.

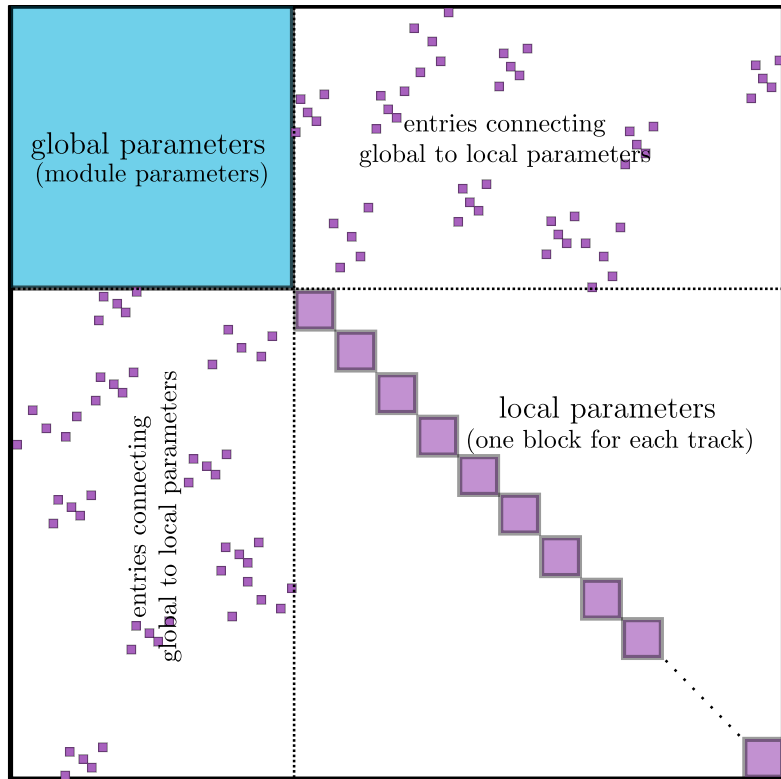


Figure 30: Track residuals.

4.2 Selected Results

CRUZET, CRAFT and first collisions of 2015

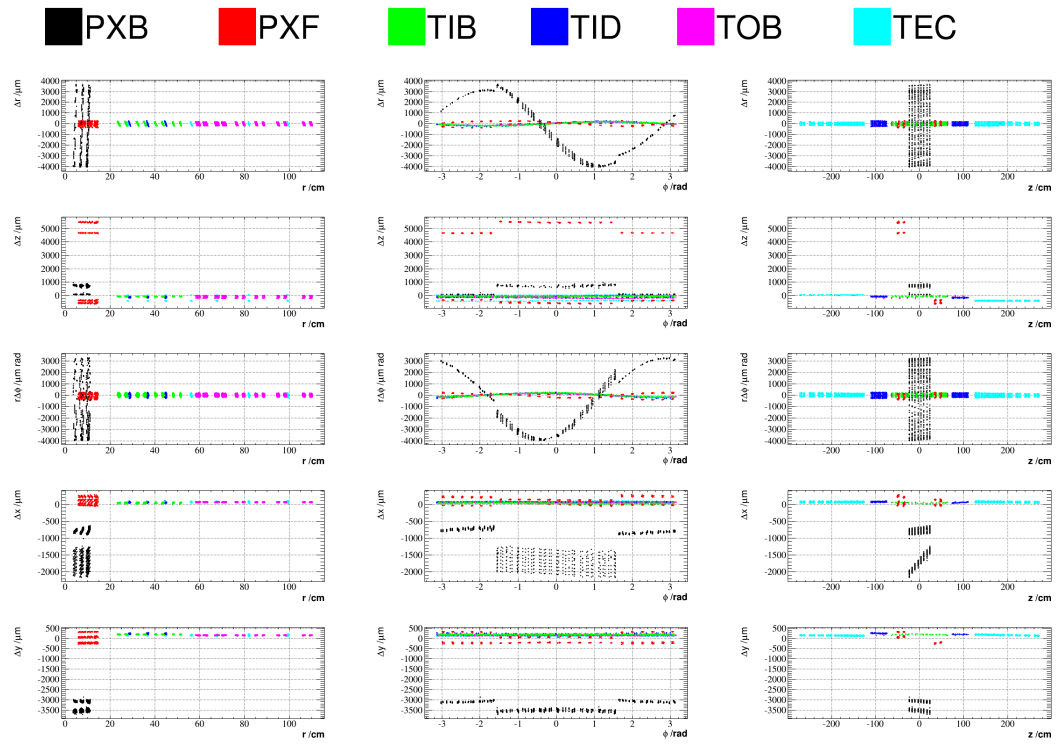


Figure 31: Geometry comparison plot of CRUZET 2015 object vs Run I.

1014 5 $W\gamma$ Cross Section Measurement

1015 Place analysis outline here

References

- [1] Griffiths textbook
- [2] website: <http://www.isgtw.org/spotlight/go-particle-quest-first-cern-hackfest>
- [3] CMS Paper about Higgs boson discovery
- [4] ATLAS Paper about Higgs boson discovery
- [5] PDG
- [6] website: <https://science.nasa.gov/astrophysics/focus-areas/what-is-dark-energy>
- [7] Pich lectures: The Standard Model of Electroweak interactions
- [8] Halzen, Martin "Quarks and leptons"
- [9] <http://iopscience.iop.org/article/10.1088/0034-4885/70/1/R02>
- [10] Peskin, Schroeder
- [11] Lindsey's thesis (CMS Zg- ζ llg, 7 TeV)
- [12] website: https://www-d0.fnal.gov/results/publications_talks/thesis/snyder/html/node17.html
- [13] website: https://en.wikipedia.org/wiki/Cross_section_%28physics%29
- [14] LO (1969) theory paper
- [15] NNLO theory paper
- [16] NLO theory paper
- [17] aTGC paper
- [18] Senka's thesis (CMS Wg- ζ munug, 7 TeV)
- [19] D0 Combination of $W\gamma$, WW, WZ and VW using 8.6 fb-1 of 2 TeV $p\bar{p}$ collisions Phys.Lett. B718 (2012) 451-459
- [20] LEP Combination of WW and single W using 0.7 fb-1 per experiment of e^+e^- collisions at WW pair production energies arXiv:1302.3415
- [21] 7TeV Wg ATLAS paper
- [22] ATLAS WW using 20.3 fb-1 of 8 TeV pp collisions Submitted to JHEP
- [23] ATLAS VW ($V=W,Z \rightarrow jj$) using 4.6 fb-1 of 7 TeV pp collisions JHEP 01 (2015) 049
- [24] website: https://twiki.cern.ch/twiki/bin/view/CMSPublic/PhysicsResultsSMPaTGC#Figure_1_Limits_on_WW
- [25] 7TeV Wg CMS paper
- [26] CMS WW using 4.9 fb-1 of 7 TeV pp collisions Eur. Phys. J. C 73 (2013) 2610
- [27] CMS WW using 19.4 fb-1 of 8 TeV pp collisions Submitted to EPJC
- [28] CMS VW ($V=W,Z \rightarrow jj$) using 5.0 fb-1 of 7 TeV pp collisions Eur.Phys.J. C73 (2013) 2283
- [29] CMS 8 TeV WW lnlnmu
- [30] CMS 7 TeV Zg nunug
- [31] CERN brochure, <http://cds.cern.ch/record/1165534/files/CERN-Brochure-2009-003-Eng.pdf>

- 1051 [32] LHC TDR
- 1052 [33] website: <http://home.cern/topics/large-hadron-collider>
- 1053 [34] website: <http://cds.cern.ch/record/1621583/files/>
- 1054 [35] http://home.cern/sites/home.web.cern.ch/files/image/update-for_cern_people/2016/06/intlumirunall_image.png
- 1055 [36] website: <http://cds.cern.ch/journal/CERNBulletin/2014/24/News%20Articles/1706606>
- 1056 [37] website: <https://twiki.cern.ch/twiki/bin/view/CMSPublic/LumiPublicResults>
- 1057